UNIVERSIDAD DE CONCEPCIÓN
FACULTAD DE CIENCIAS FÍSICAS Y MATEMÁTICAS

Analyzing protostellar evolution using MESA to understand the survival of fossil magnetic fields

Pre-main sequence evolution of intermediate mass stars

Luis Mauricio Villarroel Casanova

Tesis presentada a la Dirección de Postgrado de la Universidad de Concepción para optar al grado académico de Magíster en Astronomía

Diciembre 2025
Concepción, Chile

Profesor Guía: Dominik Schleicher

Departamento de Astronomía
Facultad de Ciencias Físicas y Matemáticas
Universidad de Concepción

A mi mamá, a mi hermano Amaro, a mi padre y a mi gato Pepito.

ACKNOWLEDGMENTS

This short academic journey was made possible thanks to the support of many people to whom I am deeply grateful.

First and foremost, I would like to thank my mother, Marisol Casanova, from my hometown of Chillán, who has always been there for me, giving everything she could to support my education and personal growth. Her constant encouragement allowed me to fully embrace and enjoy my academic experience in Concepción.

I would also like to express my heartfelt gratitude to my best friend Anajis, whose unwavering support throughout my entire academic career has been invaluable. Her presence, encouragement, and shared experiences have continuously reminded me of the importance of perseverance, companionship, and balance beyond academia.

I am grateful to my supervisor, Dr. Dominik Schleicher, for his constant guidance, insightful discussions, and for always taking the time to listen and provide support during both the scientific and personal challenges encountered throughout the development of this project. It has been a true pleasure to work under his supervision.

I wish to acknowledge Daniele Galli for the valuable discussions of the results, which provided a well-founded and insightful review of this work.

I gratefully acknowledge the financial support provided by the ANID BASAL project FB21003 (CATA), as well as the support from SOCHIAS through the Adelina Gutiérrez Fellowship, which enabled my participation in scientific activities and travel. These opportunities were essential for my professional development.

Resumen

La observación de campos magnéticos fósiles en estrellas radiativas, ha llevado al desarrollo de diferentes teorías sobre su origen. Entre ellas, la teoría de campos fósiles es un posible explicación. Sin embargo, la supervivencia de tales campos depende intrínsecamente de la estructura estelar. Nuestra meta es obtener la masa típica de la protoestrella para el cual ocurre la transición desde un estado convectivo hasta uno radiativo, ya que esto favorece fuertemente la supervivencia de estos campos magnéticos. Estudiamos la evolución en la fase de *pre-main sequence* en protoestrellas de masa intermedia usando los *Modules for Experiments in Stellar Astrophysics* (MESA), un código de evolución estelar en 1D, investigando la dependencia en la metalicidad y la tasa de acreción media, considerando diferentes escenarios. Encontramos que la transición ocurre generalmente entre ~ 1.3 $M_\odot$ y ~ 2.8 $M_\odot$ para todos los modelos estudiados y explica naturalmente que es más probable que los campos magnéticos sobrevivan en estrellas con mayor masa, como también fue encontrado en observaciones. A menor metalicidad, la transición ocurre a masas más bajas. Sin embargo, en modelos con altas tasas de acreción, los campos magnéticos acretados podrían disiparse en las capas convectivas externas. El modelo predice que la fracción de estrellas radiativas con campos magnéticos intensos debería aumentar por debajo de $Z = 0.01$.

Keywords – estrellas: campos magnéticos, formación estelar, peculiaridad química, pre-secuencia principal.

Abstract

The observation of strong magnetic fields in radiative stars has led to the development of different theories about their origin. Among them, the fossil field theory offers a possible explanation. However, the survival of such fields is intrinsically dependent on the stellar structure. Our goal is to derive the typical mass of protostars for which the transition from a convective to a radiative state occurs, as the latter will strongly favor the possible survival of magnetic fields. We study the pre-main-sequence evolution of intermediate-mass protostars using the *Modules for Experiments in Stellar Astrophysics* (MESA), a 1D stellar evolution code, investigating the dependence on metallicity and average accretion rate, considering different accretion scenarios. We find that the transition generally occurs between ~ 1.3 $M_\odot$ and ~ 2.8 $M_\odot$ for all the models studied here and it naturally explains that it is more likely that magnetic fields will survive in more massive stars, as also found in observations. At lower metallicity, this transition is found to happen at a lower mass. However, in models with high accretion rates, any accreted magnetic fields could still be dissipated in the outer convective layers. An additional prediction of our model is that the fraction of radiative stars with strong magnetic fields should increase below metallicities of $Z = 0.01$.

Keywords – stars: magnetic fields, stars: formation, stars: chemically peculiar, stars: pre-main sequence

Contents

List of Tables

List of Figures

Chapter 1

Introduction

Although humans have always looked at the stars, only recently in the history of humankind have we been able to study their properties and understand more about their formation and evolution. Thanks to the tools borrowed from physics, many brilliant minds have contributed to the formulation of a basic theory of stellar structure that provides a limited yet successful explanation for many of the observational results, helping to decipher the mysteries behind the physical processes that allow stars to shine.

The rise of computers in the post-war era brought major technological advances that have been crucial to improving our understanding of stellar physics. These developments have enabled both the observation of astrophysical objects that were impossible to detect decades ago, thanks to the new instruments, and the numerical solution of complex systems of equations within minutes with codes such as `MESA` (Paxton et al., 2011, 2013, 2015, 2019), which previously required weeks or longer to compute. In parallel, the emergence of community-driven scientific software has fundamentally transformed the interaction between stellar theory, numerical simulations, and observations (Turk et al., 2011; Foreman-Mackey et al., 2013; Ness et al., 2015; Choi et al., 2016; Astropy Collaboration et al., 2018). This paradigm shift led to a general inclination toward the formulation of equations, the calculation of numerical solutions, and the interpretation of these results, leaving aside a more formal approach to stellar physics, such as the detached analysis of the behavior of solutions[1]. As Gautschy (2018) stated, “After

---

[1] For example, the problem of the validity of the Vogt–Russell (VR) theorem.

the late 1970s, stellar-evolution research returned to and remained essentially a numerical-computation enterprise focusing on data-driven modeling." Although the formal branch of research may have diminished, the results from numerical computation have been very successful in explaining observations and predicting stellar behavior. In the following section, we review the history of the field, together with some observations and measurements that have motivated the scientific problem investigated in this work.

1.1 Brief historical introduction

Since the breakthrough period of the last century, many studies have shaped the way we understand stellar evolution today. The vast amount of successful research produced during those years led to the creation of numerous important papers and books that, despite their age, remain highly relevant. This period was marked by foundational contributions to stellar structure and nucleosynthesis, and outstanding examples are the studies by Emden (1902, 1907), in which he showed that stars can be considered as self-gravitating gas spheres governed by the laws of thermodynamics and hydrostatic equilibrium, These works are now considered an important step in the study of stellar structure. Later, Hertzsprung (1911), motivated by his interest in blackbody radiation theory, and Russell (1914) independently discovered that stars exhibit a strong correlation between apparent magnitude (or observed brightness) and spectral type. This relationship placed stars in a well-defined region of what would become the Hertzsprung–Russell diagram. Then, at the beginning of the twentieth century, Sir A. Eddington (1926) completed the theory of stellar internal structure by introducing the energy-generation and energy-transport equations into the framework previously established by Emden (1902). Furthermore, Bethe (1939) laid the groundwork for connecting the chemical evolution of stellar material with the evolutionary stages of stars by finding the fundamental nuclear reactions that sustain them throughout the main sequence (hereafter MS). Based on these milestones, subsequent decades saw major advancements driven by the influential contributions of Burbidge et al. (1957); Böhm-Vitense (1958); Schwarzschild (1958); Henyey et al. (1964); Paczyński (1970), among others, together with pioneering studies on the evolution of pre-main-sequence (hereafter PMS) stars (e.g., Larson, 1969; Baraffe et al., 1998; Palla and Stahler, 2000). Overall, these contributions have profoundly shaped the modern understanding of stellar formation and evolution, particularly in terms of their structural and thermal evolution.

However, the origin and long-term evolution of stellar magnetic fields remain less well understood. Despite the significant progress achieved in stellar evolution theory, the mechanisms responsible for the presence of strong magnetic fields in some stars are still under debate. In this context, two main theoretical frameworks have been proposed. The first considers the possibility that magnetic fields are inherited from the primordial molecular cloud and are transported into the forming star during gravitational collapse. However, the subsequent evolution of these fields throughout the protostellar phase is not yet fully understood.

1.2 Fossil magnetic fields in intermediate-mass stars

Today, with increasing observational capabilities, researchers have shown that magnetic fields are present in many astrophysical environments. In convective stars, such as M dwarfs and Sun-like stars, magnetic fields are generated and sustained by active dynamo processes. These processes generally require both rotation and convection, and therefore are more likely to operate in regions where energy transport is dominated by convection (e.g. Brandenburg and Subramanian, 2005; Käpylä et al., 2023). In the case of Sun-like stars, the magnetic field is generated by a self-excited dynamo operating within the convective layers, producing a cyclic large-scale magnetic field. Other late-type stars, such as M dwarfs, are believed to become fully convective once their masses fall below $M \approx 0.35, \mathrm{M}_{\odot}$ (Kochukhov, 2021).

In contrast, in stars with radiative envelopes and during earlier evolutionary stages, the evolution of magnetic fields may be dominated by flux freezing and amplification through compression during gravitational collapse, which is likely to govern the early dynamical evolution (Auddy et al., 2022). One of the most widely accepted hypotheses to explain the presence of strong magnetic fields in stars is the fossil field scenario. In this framework, a primordial magnetic field acquired during the collapse phase survives because its dissipation timescale exceeds the stellar evolutionary timescale, resulting in a long-lived magnetic field remnant (Dudorov and Khaibrakhmanov, 2015).

Developing a robust theory for the calculation of stellar structure and evolution is important; however, if it cannot be compared with observational results, its relevance becomes limited. An aim of the present work is to provide an initial view of these calculations compared with previous observations and then to address a deeper problem related to the formation and preservation of very strong magnetic fields observed to be inside radiative stars for long periods of time.

1.2.1 Magnetic field in radiative stars

Magnetic fields have been observed across a broad range of stellar types, including T-Tauri stars (Johns-Krull, 2007; Guenther et al., 1999; Lavail et al., 2017), low-mass main-sequence stars (Vidotto et al., 2014), and, in some cases, intermediate-mass stars with predominantly radiative envelopes (Aurière et al., 2007). Among intermediate-mass stars, particularly strong and organized magnetic fields are found in chemically peculiar objects classified as Ap/Bp stars. These stars, with masses between 1.5 and $6, \mathrm{M}_{\odot}$, possess largely radiative interiors and host stable, large-scale magnetic fields with strengths ranging from approximately 200 G to 30 kG (Aurière et al., 2007). Although Ap/Bp stars are observed during their main-sequence phase, they represent only a small fraction of the A-type star population. This rarity, combined with the presence of strong, long-lived magnetic fields in stars lacking deep convective envelopes, suggests that their magnetic fields are not generated by contemporary dynamo action, leaving their origin not yet fully understood.

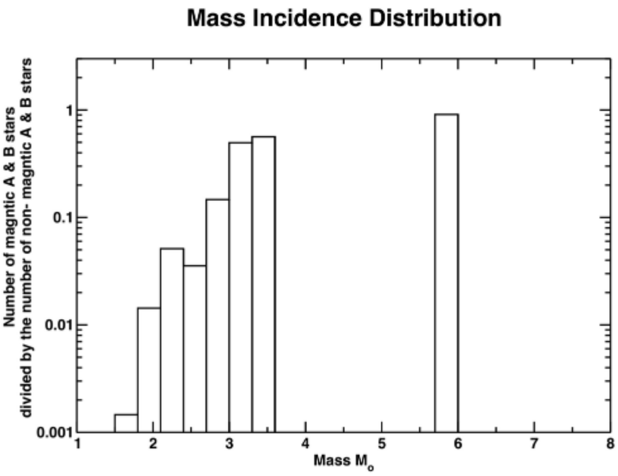

Figure 1.2.1: The fraction of intermediate-mass stars within 100 *pc* in which a magnetic field has been detected. Above 3.6 $M_{\odot}$, a sufficiently large sample of stars is not available to provide significant statistics. From Power et al. (2007).

In Fig. (1.2.1) it is shown that observations of a volume-limited sample within 100 pc from the Sun have revealed that the fraction of magnetic Ap/Bp stars increases with mass: it is below 1% at 1.5 M$_{\odot}$ and rises to $\geq$ 20% at 3.5 M$_{\odot}$. Below 1.5 M$_{\odot}$ (spectral type F0), strong magnetic fields are absent, probably due to the presence of efficient convective envelopes (Power et al., 2007). Other properties also correlate with the presence of very strong magnetic fields. In Fig. (1.2.2), Mathys (2008) shows that, Ap stars, in particular, exhibit an astonishing range of rotation periods spanning at least four orders of magnitude, and these fields are found only in stars with rotation periods shorter than 150 days. Therefore, extremely strong magnetic fields, in excess of 7.5 kG, do not occur in very slowly rotating stars, with periods longer than 150 days. Interestingly, according to Braithwaite and Spruit (2017), the chemical peculiarities seen in these stars appear to develop after the magnetic field is already in place, likely during a stage in the pre-main-sequence (hereafter PMS) phase. This suggests that the PMS phase may play a critical role in setting up the magnetic field and the chemical characteristics that we observe.

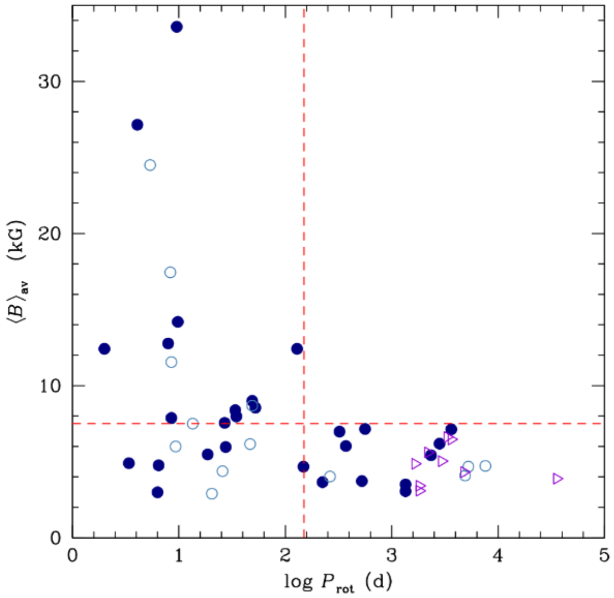

Figure 1.2.2: Observed average of the mean magnetic field modulus against rotation period. Dots: stars with known rotation periods; triangles: stars for which only the lower limit of the period is known. Open symbols are used to distinguish those stars for which existing measurements do not cover the whole rotation cycle. The horizontal and vertical dashed lines, corresponding to $\langle B \rangle_{\rm av} = 7.5\,$kG and $P_{\rm rot} = 150\,$d, respectively, emphasise the absence of very strong magnetic fields in the stars with the slowest rotation. From Mathys (2017).

In the PMS phase, protostars are classified as T Tauri stars if they are later than spectral type F5 and as Herbig Ae/Be (HAeBe) stars if they are earlier (Braithwaite and Spruit, 2017). These types of stars are typically found in regions of ongoing or recent star formation. Their position on the Hertzsprung-Russell (HR) diagram is close to the MS. Their spectra exhibit emission lines, commonly interpreted as originating from accretion disks (Donati and Landstreet, 2009). Essentially, they are precursors of MS A- and B-type stars. After a certain period, their interiors become fully radiative, meaning they no longer possess the convective layers required to sustain a dynamo mechanism, unlike their lower-mass, convective counterparts, the T Tauri stars. In Fig. (1.2.3) In a study published by Alecian et al. (2013), which examined 70 HAeBe stars, it became clear that a fraction of these stars exhibit magnetic fields. This suggests a different origin for these fields, as traditional dynamo action is not expected in fully radiative stars.

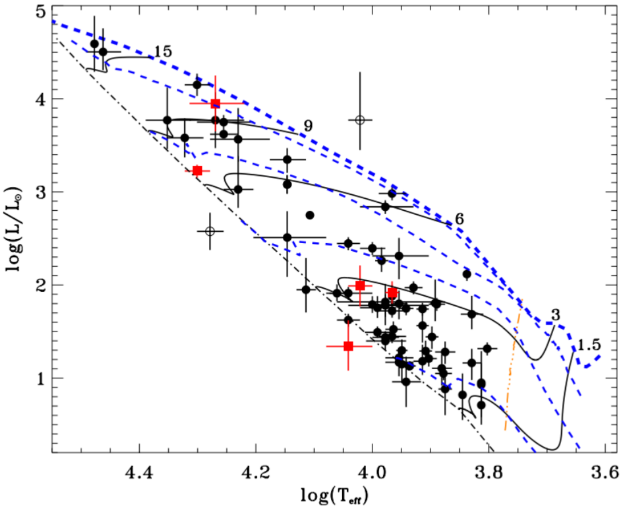

Figure 1.2.3: Magnetic (**red squares**) and non-magnetic (**black points**) Herbig Ae/Be stars plotted in a Hertzsprung-Russell diagram. The **thick blue dashed** line is the birth line, the **thin blue dashed** lines are isochrones, the dot-dashed line is the ZAMS and the solid lines are theoretical evolutionary tracks from the birth line to the ZAMS for the masses indicated. The **orange dot-dot-dot-dashed** line represents a convective/radiative transition: to the left of this line, the convective envelope accounts for less than 1% of the star's mass. From Alecian et al. (2013).

1.2.2 Magnetic fields in star-forming clouds

Observational results have established that there is a correlation between the magnetic field strength B and the numerical density of clouds n, for star-forming clouds, given as

$$\frac{B}{B_0} = \left(\frac{n}{n_0}\right)^k . \tag{1.2.1}$$

Here, B_0 and n_0 depend on the cloud formation conditions. For a density range between 1 and 10^{10} cm^{-3}, a large part of the observational data can be described with the following parameters,

$$B_0 = 5\mu G, n_0 = 50 - 200 \text{ cm}^{-3}, k = 1/2 - 2/3. \tag{1.2.2}$$

This is confirmed by optical and infrared polarimetry of dense molecular and protostellar clouds (Vallee, 1997; Girart et al., 2006; Li et al., 2009; Crutcher, 2012; Chapman et al., 2013; Koley et al., 2022). A comparison of the observed magnetic flux for radiative stars and interstellar molecular clouds suggests that star formation occurs in magnetized clouds. Hence, the magnetic flux of young and some MS stars may be a relic of molecular or protostellar clouds, implying a fossil origin (Dudorov and Khaibrakhmanov, 2015). Several numerical simulations have been carried out to study the evolution of the magnetic field strength during gravitational collapse, with initial strengths of $30 - 300\ \mu G$ at a number density of 300 cm^{-3}. When molecular clouds collapse, the magnetic field strength increases as the density of the gas rises, leading to a central field strength of about $0.1\ G$ at a number density in the range of $10^{10} - 10^{11}$ cm^{-3} (Desch and Mouschovias, 2001; Nakano et al., 2002; Tomida et al., 2015; Masson et al., 2016). However, there is a point at which the field stops increasing and is no longer efficiently coupled to the gas, and remains approximately constant while the gas increases towards protostellar densities of $10^{15} - 10^{16}$ cm^{-3}, due to a drop in the degree of ionization and a decoupling of the magnetic field from the gas. Only when the temperature rises sufficiently to ionize the gas does the magnetic field couples again to the gas (Nakano, 1988; Nakano and Umebayashi, 1988). The fields that are amplified in this way may be accreted onto protostars and may become the fossil fields observed in Ap/Bp-type stars.

1.3 Thesis outline

In this work, we aim to determine when and under what conditions protostars undergo a relevant radiative phase, as such a stage considerably increases the likelihood of magnetic field survival. This is particularly important because accretion onto protostars is typically a continuous process and is very likely to proceed even after this transition. Here, we explore protostellar evolution considering different accretion scenarios, including constant, decaying, and oscillating accretion rates. We computed the protostellar evolution for a $1\mathrm{M}_{\odot}$ star using Modules for Experiments in Stellar Astrophysics (MESA; Paxton et al. 2011, 2013, 2015, 2019; Jermyn et al. 2023), a widely used 1D stellar evolution code, particularly well suited for this purpose. With these simulations, we quantify the protostellar mass at which the transition from a convective to a radiative interior occurs, which we analyze as a function of the mean accretion rate and under different assumptions regarding the time dependence of the accretion rate and the metallicity. The remainder of this work is organized as follows. In Chapter 2, we introduce the theoretical framework used in this project, describing the fundamental equations of stellar structure and the dynamics of magnetic fields, which give rise to the two main theories proposed to explain the strong magnetic fields observed in stars. Chapter 3 presents the methodology adopted in this work, explaining how the equations are solved using the `MESA` code and detailing the numerical setup and criteria employed. In Chapter 4, we review and compare the results obtained for the three different accretion rate prescriptions and analyze their respective dependencies. Finally, Chapter 5 summarizes the main conclusions and discusses the implications of our findings. Additional data and supplementary plots from the simulations are provided in the Appendix A.

Chapter 2

Theoretical framework

Stars play a crucial role in our understanding of material formation, as they are responsible for producing the heavy elements that enrich their surroundings through nucleosynthesis and associated dynamical feedback. Moreover, stars are relevant in a wide range of research areas, including the detection and characterization of exoplanets, the study of stellar clusters, supernovae, and the formation and structure of the Milky Way and other galaxies. All of these fields rely on a fundamental pillar: the accuracy of the theory of stellar structure and evolution. Nonetheless, despite the fact that the general picture of stellar structure and evolution is well established, important shortcomings remain. In particular, the effects of rotation, binary interactions, and magnetic fields are often simplified or neglected and still need to be addressed in detail. The following sections are mainly based on the book by Kippenhahn et al. (2012) and on the lecture notes by Warrick Ball, Jørgen C-D and Onno Pols.

2.1 Stellar structure and evolution

To formulate a theory of stellar structure that is computationally feasible, it is necessary to introduce simplifying assumptions. First, a star is treated as a fluid, since its internal behavior can be described through the equations of fluid dynamics. The structure is then assumed to depend only on a chosen independent coordinate (the enclosed mass in a given shell in this case), which implies that the star is not rotating. The star is also considered self-gravitating, meaning that no external forces act on the system other than gravity, so electric and magnetic fields are not included in the fluid equations. Another assumption is that the star is stationary on dynamical timescales, so net velocities and accelerations are neglected. Finally, the condition of local thermal equilibrium is adopted, which means that each mass shell is characterized by a well-defined temperature within an infinitesimal neighborhood. As a further assumption, particle velocities are taken to follow Maxwellian distributions, while the radiation field is described as a blackbody at the same local temperature.

Then, to describe the non-linear partial differential equations (NL-PDEs) that describe the stellar structure, one has to know first that the pressure and density of the material depends on the distance to the center of the star but not as a function of the radius; instead, the independent variable is chosen as a Lagrangian variable, since density is always positive, the function for the mass m_r enclosed by a certain radius r is monotonic, where $m_{r=\mathrm{cen}} = 0$ at the center and $m_{r=\mathrm{surf}} = M_*$ at the surface. In the second place, the problem consists in determining the functions for radius $r(t, m_r)$, pressure $P(t, m_r)$, luminosity $L_r(t, m_r)$, temperature $T(t, m_r)$ and chemical composition $X_i(t, m_r)$, where the subscript i indicates the chemical species and $\sum X_i = 1$. These solutions are governed by the stellar structure NL-PDEs given by:

The continuity equation,

$$\frac{\partial r(t, m_r)}{\partial m_r} = \frac{1}{4\pi r(t, m_r)^2 \rho(t, m_r)} \tag{2.1.1}$$

the momentum equation, where in hydrostatic equilibrium the second term vanishes since $\partial_t^2 r = 0$,

$$\frac{\partial P(t, m_r)}{\partial m_r} = -\frac{G m_r}{4\pi r(t, m_r)^4} + \frac{1}{4\pi r(t, m_r)^2}\frac{\partial^2 r(t, m_r)}{\partial t^2} \tag{2.1.2}$$

the energy equation,

$$\frac{\partial L_r(t, m_r)}{\partial m_r} = \epsilon_{\mathrm{nuc}}(t, m_r) - \epsilon_\nu(t, m_r) + \epsilon_{grav}(t, m_r) \tag{2.1.3}$$

the temperature gradient equation,

$$\frac{\partial T(t, m_r)}{\partial m_r} = -\frac{G m_r T(t, m_r)}{4\pi r(t, m_r)^4 P(t, m_r)} \nabla(t, m_r) \tag{2.1.4}$$

and the composition equations,

$$\frac{\partial X_i(t,m_r)}{\partial t} = \frac{m_i}{\rho}\left(\sum_j r_{ji}(t,m_r) - \sum_k r_{ik}(t,m_r)\right) \tag{2.1.5}$$

These equations form the fundamental basis for stellar modeling. Equation (2.1.1) represents the conservation of mass within the star. It relates the radial variation of the enclosed mass to the local density and ensures that mass is neither created nor destroyed as one moves through the stellar interior. In the context of one-dimensional, spherically symmetric stellar structure, this equation defines how the total mass is built up from the center outward and provides the mass coordinate that is commonly used as the independent variable in stellar evolution calculations. Equation (2.1.2) describes the dynamical balance between the gas and radiation pressure acting against gravity. This equation of motion reaches hydrostatic equilibrium when these forces balance each other, which is a direct consequence of the conservation of linear momentum, with G denoting the gravitational constant. These two equations define what is called the mechanical structure of the star, since thermal physics is not applied yet. This structure can be solved at this stage if the pressure P is purely a function of the density ρ, as is the case for polytropes. Equation (2.1.3) defines the energy content of a star at a given mass shell ∂m as the combined contribution of nuclear energy generation ϵ_{nuc} and the change of internal energy due to expansion or contraction ϵ_{grav} (equal to $dQ = TdS/dt$ by definition), reduced by the energy loss rate due to neutrino flux ϵ_ν, which clearly represents the conservation of energy. Equation (2.1.4) describes the energy transport within the star, where hydrostatic equilibrium is also assumed. When modelling a star, the dimensionless temperature gradient is defined as $\nabla = d\ln T/d\ln P$ for a given process, which represents the variation of temperature with depth, where pressure acts as a measure of depth. The expression for this gradient depends on the energy transport mechanism operating in the local regions of the stellar interior. Equation (2.1.5) defines the time variation of the mass fraction X_i of the i-th chemical species of mass m_i, produced or destroyed by thermonuclear reaction rates denoted by r_{ji} (converting particles j into i) and r_{ik} (converting particles i into k). When the evolution of the stellar structure is slow compared to changes in composition, this equation can be decoupled from the others, allowing the general structure to be solved at a given time t for a fixed composition X_i.

In addition to these equations, stellar evolution calculations also require equations for the thermodynamic properties of the stellar matter, this is a set of matter equations, which are not computed *a priori* within stellar evolution codes. Instead, the corresponding data are provided in tabulated form. These tables are produced by specialized research groups that perform detailed microphysical calculations and compile the results so that stellar evolution codes can interpolate the required quantities at any given point inside the star.

These relations can be written as

$$\begin{aligned} \kappa &= \kappa(\rho, T, X_i), && (2.1.6) \\ \epsilon_{\text{nuc}} &= \epsilon_{\text{nuc}}(\rho, T, X_i), && (2.1.7) \\ \epsilon_{\nu} &= \epsilon_{\nu}(\rho, T, X_i), && (2.1.8) \\ R_{ij} &= R_{ij}(\rho, T, X_i), && (2.1.9) \end{aligned}$$

where κ is the opacity, ϵ_{nuc} is the nuclear energy generation rate, ϵ_{ν} represents the energy losses due to neutrino emission, and R_{ij} denotes the nuclear reaction rates between species i and j.

Together with these relations, the equation of state completes the full set of equations required to describe the stellar interior. The equation of state, in its simplest form, relates pressure as a function of density, temperature, and chemical composition. In the most general case, however, it may include a wide variety of thermodynamic variables and non-ideal effects.

$$P = P(\rho, T, X_i) \tag{2.1.10}$$

With the increase in computational power, analytical approximations to the equation of state have become less accurate than modern tabulated data that codes interpolate, which incorporate detailed microphysics and provide significantly improved accuracy across a wide range of stellar conditions.

2.1.1 Radiative energy transport

One of the two main mechanisms for energy transport in stars is via photons, that is, radiative transport. The treatment of radiative energy transport is complex, as it involves the interaction between matter and radiation, especially when dealing with stellar atmospheres. Radiative transfer is in fact a complete field of research. However, in the stellar interior a simplified description is sufficient, where the transport of radiation can be treated within the diffusion approximation. This approximation assumes that the photon mean free path is much smaller than the stellar radius, so photons are scattered, absorbed, and re-emitted many times before escaping. This assumption breaks down near the stellar surface. Regions where the diffusion approximation holds are usually referred to as optically thick. In this regime, the radiative flux can be described by a diffusion law analogous to the well-known *Fick's law*, which is given by

$$\boxed{\boldsymbol{j} = -D\boldsymbol{\nabla} n}\,, \quad \text{with } D = \frac{1}{3}v\ell_p \tag{2.1.11}$$

where $\boldsymbol{j}$ is the diffusive flux of particles between regions of different particle density n, and D is the diffusion coefficient, calculated using the average values of the particle velocity v and the mean free path ℓ_p of the particles.

To obtain the diffusive flux of radiative energy, we replace $\boldsymbol{j} \to \boldsymbol{F}_v$ in the frequency interval $[v, v+dv]$, the particle density by the radiation energy density, $n \to u_v(T)$, the mean particle velocity by the speed of light, $v \to c$, and the mean free path by the photon mean free path, $\ell_p \to \ell_{ph,v}$. This yields

$$\boxed{\boldsymbol{F}_v = -D_v\boldsymbol{\nabla} u_v}\,, \quad \text{where } D_v = \frac{1}{3}c\ell_{ph,v} = \frac{c}{3\kappa_v\rho}. \tag{2.1.12}$$

The radiation energy for a specific frequency (for all frequencies $u(T) = aT^4$) is given by

$$u_v(T) = \frac{4\pi}{c}B_v(T) = \frac{8\pi h}{c^3}\frac{v^3}{e^{hv/kT}-1}. \tag{2.1.13}$$

Integrating Eq. (2.1.12) over frequency and assuming spherical symmetry, such that $F_r = |\boldsymbol{F}| = F_{\mathrm{rad}}$ and $\boldsymbol{\nabla} = (\partial u_v/\partial r)\hat{r}$, one obtains

$$\int F_v dv = -\int D_v \frac{\partial u_v}{\partial r} dv \tag{2.1.14}$$

$$F_{\mathrm{rad}} = -\frac{4acT^3}{3\rho\kappa_R}\frac{\partial T}{\partial r}, \tag{2.1.15}$$

where κ_R is the Rosseland mean opacity, ρ is the density, $a = 4\sigma/c$ is the radiation density constant, and c is the speed of light. Then, expressing the radiative flux in terms of the local luminosity, $L = 4\pi r^2 F_{\mathrm{rad}}$, and solving for the temperature gradient, one obtains

$$\left(\frac{\partial T}{\partial r}\right)_{rad} = -\frac{3}{16\pi ac}\frac{\kappa_R \rho L}{r^2 T^3}. \tag{2.1.16}$$

In addition, Eq. (2.1.15) can be interpreted as an equation for heat conduction by writing

$$\boxed{\boldsymbol{F}_{\mathrm{rad}} = -k_{\mathrm{rad}}\boldsymbol{\nabla}T}\,, \quad \text{with } k_{\mathrm{rad}} = \frac{4acT^3}{3\rho\kappa_R}, \tag{2.1.17}$$

where k_{rad} represents the radiative conductivity coefficient.

In stellar modelling, it is useful to define the dimensionless temperature gradient, using (2.1.16) and (2.1.2) assuming hydrostatic equilibrium, as

$$\begin{aligned}\nabla_{\mathrm{rad}} = \left(\frac{d\ln T}{d\ln P}\right)_{rad} = \frac{P}{T}\frac{dT}{dr}\frac{dr}{dP} &= \frac{P}{T}\left(-\frac{3}{16\pi ac}\frac{\kappa_R\rho L}{r^2T^3}\right)\left(-\frac{r^2}{Gm\rho}\right)\\ &= \frac{3\kappa}{16\pi acG}\frac{LP}{mT^4},\end{aligned} \tag{2.1.18}$$

where "*rad*" denotes that this is the gradient required to transport all the energy by radiation. Hence, Eq.(2.1.16) can be re-written as

$$\frac{\partial T}{\partial m} = -\frac{GmT}{4\pi r^4 P}\nabla_{\mathrm{rad}} \tag{2.1.19}$$

which is the same as Eq. (2.1.4) with $\nabla = \nabla_{rad}$.

2.1.2 Convective energy transport

Convective transport takes place when the opacity and the energy flux are too large to be carried by radiation alone, making radiative transport inefficient and unable to sustain stable energy transfer. This type of transport occurs when fluid elements exchange energy while moving from hotter to cooler regions in a dynamically unstable layer. Hot parcels of material rise, while cooler ones sink. Since the density becomes very high near the stellar core, convection is particularly efficient in that region. A complete description of this motion is not yet well understood, and a formulation based on first principles does not exist, because the hydrodynamical motions involved are extremely complex, even in a simple system such as boiling water in a kettle. To solve the equations of stellar structure under these conditions, one must adopt a convection theory to determine the extent to which heat is transported by convective motions. Several attempts have been made to describe this process, but one of the longest-standing and most commonly used frameworks in stellar models is the remarkably simple mixing length theory (MLT), which provides a local treatment of convection and yields a good approximation in regions near the stellar core. It assumes hydrostatic equilibrium and that convection is time-independent.

2.1.2.1 Mixing-length theory

As reviewed by Gough and Weiss (1976), the historical development of mixing-length ideas can be traced back to early hydrodynamical work in the first half of the 20th century. Several pioneers, including Taylor (1915), Schmidt (1917) and Prandtl (1925), introduced the fundamental concept of a fluid element traveling a characteristic distance, the mixing length ℓ, before losing its identity through turbulent dissipation. These ideas were later adapted to astrophysical applications, most notably by Biermann (1932, 1945), who considered the adiabatic motion of rising and sinking fluid parcels with a characteristic size of order ℓ. Using this framework, he inferred properties of the solar convection zone by comparing ℓ with the observed size of photospheric granules, obtaining a scale of approximately 100 000 km (Biermann, 1938). The *mixing-length theory* (hereafter MLT) formalism that became standard in stellar evolution calculations was formulated by Böhm-Vitense (1958), and her prescription remains the most widely used today. Nevertheless, alternative formulations, often referred to as

MLT-*flavours*, have been proposed, such as the one formulated by Cox and Giuli (1968) and many others that consider different assumptions and have different applications.

The theory treats convection as rising and falling parcels of material (also referred to as *eddies*, *bubbles*, *blobs*, or simply *convective elements*) in a chemically homogeneous region inside the star, perturbed upward adiabatically, that is, without exchanging heat with their surroundings. As the blob rises, it expands because it is hotter than the surrounding material, while pressure equilibrium is assumed. Depending on the density gradient, the surrounding gas may or may not be denser than the blob. The characteristic distance that the blob travels upward or downward before dissolving into its surroundings is called the mixing length ℓ_{MLT} (often denoted as Λ), which is usually taken to be proportional to the (local) *pressure scale height* H_p, which is defined as:

$$H_p \equiv -\frac{dr}{d\ln P} = -P\frac{dr}{dP} = \frac{P}{\rho g} \tag{2.1.20}$$

where the last expression is only valid under hydrostatic equilibrium and g is the local gravitational acceleration. Hence, for any stellar model the mixing length is assumed to be as follows:

$$\ell_{MLT} = \alpha_{MLT} H_p, \tag{2.1.21}$$

where α_{MLT} is a constant of proportionality (the main free parameter) determined by calibrating stellar models to the Sun, it sets the efficiency of convection and it is taken to be constant for all stars.

2.1.2.2 Convective instability

From this picture, we obtain a condition of instability. If the surroundings are less dense than the blob, it will sink after the perturbation, returning to its initial position. Conversely, if the surroundings are denser, the blob continues rising due to its positive buoyancy. The last one is unstable and is known as convective instability, and the condition for its onset is given by the *Schwarzschild criterion*:

$$\nabla_{rad} > \nabla_{ad} \tag{2.1.22}$$

However, if the chemical composition inside the star is not homogeneous, the *Ledoux criterion* must be used instead, given by

$$\nabla_{rad} > \nabla_{ad} + \frac{\phi}{\delta}\nabla_{\mu} \tag{2.1.23}$$

Here, $\nabla_{ad} = (d\ln T/d\ln P)_{ad}$ is the adiabatic temperature gradient, where adiabatic means that changes in T with respect to P are at constant entropy, and $\nabla\mu = d\ln\mu/d\ln P$ is the mean molecular weight (composition) gradient, which has a stabilizing effect. If there is an equality in these equations we obtain the marginal stability. The thermodynamic derivatives that accompany ∇_{μ} are defined as:

$$\delta := -\left(\frac{\partial\ln\rho}{\partial\ln T}\right) = -\left(\frac{T}{\rho}\frac{\partial\rho}{\partial T}\right), \qquad \phi := \left(\frac{\partial\ln\rho}{\partial\ln\mu}\right) = \left(\frac{\mu}{\rho}\frac{\partial\rho}{\partial\mu}\right), \tag{2.1.24}$$

Where these partial derivatives correspond to constant values of T, μ and P, μ, respectively. If the ideal gas approximation is adopted, with $\rho \approx P\mu/T$, then $\delta = \phi = 1$. It should be noted that in a chemically homogeneous interior, $\nabla\mu = 0$, and the inequality from (2.1.22) is recovered.

In regions that are locally stable against convection, the inequalities in (2.1.22) and (2.1.23) are reversed. When the stability condition is satisfied, the buoyancy force pushes the displaced fluid parcels back toward their equilibrium position. However, when a parcel overshoots, it begins to oscillate around this point with a characteristic frequency called the Brunt–Väisälä frequency N, defined as

$$N^2 = \frac{g}{H_P}\left(\nabla_{ad} - \nabla + \nabla_{\mu}\right), \tag{2.1.25}$$

where $g = Gm/r^2$ is the local gravitational acceleration. A positive value of N^2 indicates stable oscillations (radiative or semiconvective zones), while a negative value implies exponential growth of the displacement, leading to convective instability.

2.1.2.3 Convective flux

Considering that the total flux of a star is given by $F_{\text{total}} = F_{\text{rad}} + F_{\text{conv}}$, and using (2.1.18), the radiative gradient required to transport the entire flux by radiation alone is

$$F_{\text{rad}} + F_{\text{conv}} = \frac{4acG}{3}\frac{T^4 m}{\kappa P r^2}\nabla_{\text{rad}}. \tag{2.1.26}$$

However, when part of the flux is carried by convection, the radiative component decreases because the actual temperature gradient ∇ becomes smaller than ∇_{rad}. This reduction occurs because radiation is responsible for transporting only a fraction of the total flux. In this case, the radiative flux is

$$F_{\text{rad}} = \frac{4acG}{3}\frac{T^4 m}{\kappa P r^2}\nabla. \tag{2.1.27}$$

If the total flux were transported exclusively by radiation, then $F_{\text{conv}} = 0$ and $\nabla = \nabla_{\text{rad}}$ would follow immediately. In general, however, ∇ is not known a priori, and therefore an expression for the convective flux becomes necessary. To obtain F_{conv}, several assumptions must be introduced, leading to the expression

$$\begin{aligned} F_{\text{conv}} &= \rho c_P v D T & (2.1.28)\\ &= \rho c_P T \sqrt{g\delta}, \frac{\ell_{\text{MLT}}}{4\sqrt{2}} H_P^{-3/2}(\nabla - \nabla_e)^{3/2}. & (2.1.29) \end{aligned}$$

Here we have used the expression for the average velocity of the convective elements as they rise through the medium,

$$v = g\delta(\nabla - \nabla_{\text{ad}})\frac{\ell^2_{\text{MLT}}}{8H_P}, \tag{2.1.30}$$

and the following relation provides an expression for the difference between the stratification gradient and the gradient inside the convective elements,

$$\frac{\nabla_e - \nabla_{\text{ad}}}{\nabla - \nabla_e} = \frac{6acT^3}{\kappa \rho^2 c_P v \ell_{\text{MLT}}}. \tag{2.1.31}$$

With the set of equations (2.1.26), (2.1.27), (2.1.28), (2.1.30), and (2.1.31), one can solve simultaneously for the convective flux F_{conv}, the radiative flux F_{rad}, the convective velocity v, the actual stratification gradient ∇, and the temperature gradient inside the convective elements, ∇_e. This procedure is possible when the local magnitudes P, T, ρ, L, m, c_p, ∇_{rad}, ∇_{ad}, and g are specified. Under these conditions, one can apply MLT (2.1.2.1), to compute all the remaining quantities of interest.

2.1.3 Kippenhahn diagrams

These diagrams are named after the astrophysicist Rudolf Kippenhahn, in recognition of his contributions to the computation of stellar structure and evolution (Kippenhahn et al., 2012). They are commonly used to visualize the internal structure of stars derived from the stellar structure equations and are known as Kippenhahn diagrams. These two-dimensional plots map the stellar interior and show how the boundaries between different regions of the star evolve over time, including sites of nuclear energy generation, shell-burning regions, and the dominant modes of energy transport. Such information is essential for understanding stellar evolution.

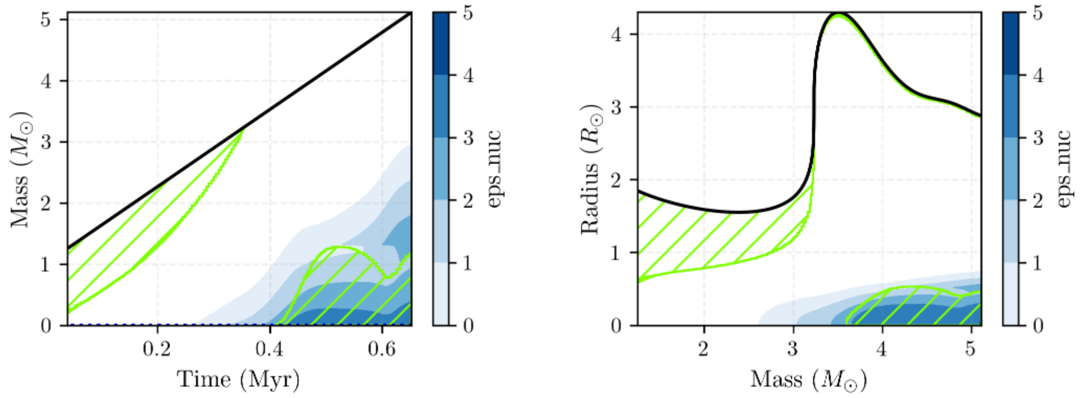

(a) Kippenhahn diagram showing the evolution of a star, with time on the horizontal axis and enclosed mass on the vertical axis.

(b) Kippenhahn diagram showing the evolution of a star, with increasing mass on the horizontal axis and radius on the vertical axis.

Figure 2.1.1: Examples of Kippenhahn diagrams showing the pre-main-sequence structure of a star with solar metallicity, an initial mass of $1, \mathrm{M}_\odot$ and a constant accretion rate of $\dot{M} = 10^{-6}$ $\mathrm{M}_\odot$/yr are presented. These models are evolved until they reach the ZAMS phase. Green regions indicate the convectively unstable parts of the star, while empty regions correspond to radiative zones. The color bar represents the energy generation rate in the central core. As the mass increases, one can observe how the internal structure of the star changes over time as the convective boundaries evolve. In particular, the convective envelope becomes progressively shallower, and at a certain point the stellar core becomes convective.

Typically, the x-axis represents the stellar age or mass, although it may also correspond to other quantities, the only condition is that it has to define a sequence of models, such as the model number in MESA calculations. The y-axis usually represents either the radius or the enclosed mass coordinate. One commonly plots the mass coordinates of the boundaries of convective zones, as well as the locations of significant nuclear energy generation. In this way, Kippenhahn diagrams, as shown in Fig. (2.1.1), allow one to clearly identify where convection or radiative transport occurs inside the star, where nuclear burning takes place, and how all these features change over time.

2.2 Magnetohydrodynamics

A large majority of the observed stellar properties can be explained within the framework of the classical theory of stellar structure and evolution, but is far from being complete, and an additional level of complexity is added by the presence of magnetic fields, observed in many types of stars. Hence, there has been increasing interest in the presence of magnetic fields in stellar interiors, motivated by advances in asteroseismology and numerical simulations. More recently, discrepancies between theoretical predictions and increasingly precise observations have highlighted the need for improved stellar evolution models that include internal magnetic fields. Such models are required to account for the strong magnetic fields observed in some chemically peculiar stars, as already discussed in Chapter 1.

In order to study these magnetic fields, the preferred theoretical framework is non-ideal magnetohydrodynamics (hereafter MHD). This field of research combines classical electromagnetism, which describes electric currents, electric fields, and magnetic fields, with fluid mechanics, which governs the motion of liquids and gases and the forces acting on them. When studying fluids, electromagnetic effects are often neglected. However, when the fluid is electrically conducting, additional considerations must be taken into account. In the presence of electric and magnetic fields, electric currents are induced by the motion of the fluid through the magnetic field, while the forces acting on the fluid are in turn modified by these currents and magnetic fields. MHD aims to describe the coupled and self-consistent interaction between fluid motion and electromagnetic fields arising from these processes. The following Section is mainly based on the studies of Braithwaite and Spruit (2017) and the book written by Choudhuri (1998).

2.2.1 Introduction

The evolution of a magnetized fluid is described by a set of equations that combine the equations of hydrodynamics with Maxwell's equations. The complete formulation depends on the specific characteristics of the astrophysical system, such as viscosity, resistivity and other microphysical processes. In the ideal case, these additional effects are neglected. The set of equation that describes the evolution of of this fluis are given by the following:

The mass conservation is expressed through the continuity equation,

$$\frac{\partial \rho}{\partial t} = -\nabla \cdot (\rho \mathbf{v}), \tag{2.2.1}$$

which ensures that any temporal change in density is balanced by the divergence of the mass flux.

The conservation of momentum, is described by the equation of motion,

$$\rho \frac{\partial \mathbf{v}}{\partial t} = -\rho(\mathbf{v} \cdot \nabla)\mathbf{v} - \nabla P + \mathbf{j} \times \mathbf{B} + \mathbf{F}_g + \mathbf{F}_v, \tag{2.2.2}$$

where the fluid acceleration results from the combined action of inertial terms, pressure gradients, magnetic forces, gravity, and viscous stresses.

The evolution of the internal energy of the fluid is given by the energy equation,

$$\rho \frac{D\epsilon}{Dt} = -P\nabla \cdot \mathbf{v} + \nabla \cdot (\kappa \nabla T) + L_r + \frac{j^2}{\sigma} + H, \tag{2.2.3}$$

which accounts for compressional work, thermal diffusion, radiative energy exchange, Ohmic dissipation, and additional heating processes.

The temporal evolution of the magnetic field is governed by the induction equation,

$$\frac{\partial \mathbf{B}}{\partial t} = \nabla \times (\mathbf{v} \times \mathbf{B} - \eta \nabla \times \mathbf{B}), \tag{2.2.4}$$

describing the competition between magnetic field advection by the flow and diffusion due to finite electrical conductivity.

In these equations, ρ denotes the mass density, $\mathbf{v}$ the velocity of the plasma flow, P the gas pressure, $\mathbf{B}$ the magnetic field, $\mathbf{j}$ the electric current density, and ϵ the specific internal energy per unit mass. The operator $D/Dt = \partial/\partial t + \mathbf{v}\nabla$ represents the Lagrangian time derivative, T is the temperature, κ the thermal conductivity or rate of heat flow, σ the electrical conductivity, and η the magnetic diffusivity, which measures the diffusion of the magnetic fields. The terms $\mathbf{F}_g$ and $\mathbf{F}_v$ correspond to gravitational force acting on the plasma and viscous forces due to fluid movement per unit volume, respectively, while L_r represents radiative heating or cooling function and H accounts for sources of heating.

2.2.2 The induction equation

Besides the importance of the set of equations presented in the previous section, the main focus of this thesis is the induction equation, since it governs the evolution of the magnetic field and allows us to address the origin of the strong magnetic fields observed in some stars. The first objective is therefore to derive this equation, which will later be applied in an astrophysical context.

The transformation laws for the electromagnetic fields $\mathbf{E}$ and $\mathbf{B}$ follow well defined rules. Assuming that the plasma moves with a velocity $\mathbf{v}$, the fields $\mathbf{E}'$ and $\mathbf{B}'$ are related to $\mathbf{E}$ and $\mathbf{B}$ as follows

$$\begin{aligned}
E'_{||} &= E_{||}, && (2.2.5)\\
B'_{||} &= B_{||}, && (2.2.6)\\
\mathbf{E}'_{\perp} &= \gamma\left(\mathbf{E}_{\perp} + \frac{\mathbf{v}}{c} \times \mathbf{B}_{\perp}\right), && (2.2.7)\\
\mathbf{B}'_{\perp} &= \gamma\left(\mathbf{B}_{\perp} - \frac{\mathbf{v}}{c} \times \mathbf{E}_{\perp}\right), && (2.2.8)\\
\gamma &= \frac{1}{\sqrt{1 - v^2/c^2}}, && (2.2.9)
\end{aligned}$$

where γ is the Lorentz factor, c is the speed of light, and the symbols $||$ and $\perp$ denote the directions parallel and perpendicular to $\mathbf{v}$, respectively.

A common approximation in this context is to retain only terms of order $|\mathbf{v}|/c$ and neglect terms of order v^2/c^2, which implies $\gamma \simeq 1$. Under this approximation, Eqs. (2.2.5) and (2.2.7) can be combined to give

$$\mathbf{E}' \;=\; \mathbf{E} + \frac{\mathbf{v}}{c} \times \mathbf{B}. \tag{2.2.10}$$

Using Ohm's law, written as Eq. (2.2.11), it follows that the electric current density inside a conducting medium is proportional to the electric field, namely

$$\begin{aligned} \mathbf{J} \;&=\; \sigma\left(\mathbf{E} + \frac{\mathbf{v}}{c} \times \mathbf{B}\right) && (2.2.11) \\ &=\; \sigma\mathbf{E}', && (2.2.12) \end{aligned}$$

where $\sigma = 1/\eta$ is the electrical conductivity.

For very large values of the electrical conductivity, the plasma can be considered highly conducting. In this limit, the current density remains finite only if the electric field in the comoving frame, $\mathbf{E}'$, is very small. From Eq. (2.2.10), it is then straightforward to show that, in the limit $\mathbf{E}' \to 0$, the magnitudes of the fields satisfy $|\mathbf{E}| \approx |\mathbf{B}||\mathbf{v}|/c$.

On the other hand, by performing the same analysis for the transformation laws of the magnetic field, Eqs. (2.2.6) and (2.2.8) can be combined to obtain

$$\mathbf{B}' \;=\; \mathbf{B} - \frac{\mathbf{v}}{c} \times \mathbf{E}. \tag{2.2.13}$$

Taking into account that $|\mathbf{E}| \approx |\mathbf{B}||\mathbf{v}|/c$ and neglecting terms of order v^2/c^2, the correction term on the right hand side is of second order and can therefore be ignored. As a result, the magnetic field is approximately invariant under the transformation, yielding

$$\mathbf{B}' = \mathbf{B}. \tag{2.2.14}$$

Equations (2.2.10) and (2.2.14) thus give the reduced transformation laws in the non relativistic limit. From the *Ampere-Maxwell law*

$$\boldsymbol{\nabla} \times \mathbf{B} = \frac{4\pi}{c}\mathbf{J} + \frac{1}{c}\frac{\partial \mathbf{E}}{\partial t}. \tag{2.2.15}$$

It can be seen that the displacement current must be neglected when terms of order v^2/c^2 are discarded. Taking l as a typical length scale, t as a typical time scale, and assuming the characteristic velocity to be of order $v \sim l/t$, one finds that the ratio between the displacement current and the conduction current is of order

$$\frac{\frac{1}{c}\frac{\partial \mathbf{E}}{\partial t}}{|\boldsymbol{\nabla} \times \mathbf{B}|} \approx \frac{\frac{1}{c}\frac{|E|}{t}}{\frac{|B|}{l}} \approx \frac{|v|}{c}\frac{|E|}{|B|} \approx \frac{v^2}{c^2} \ll 1, \tag{2.2.16}$$

which reduces Eq. (2.2.15) to

$$\boldsymbol{\nabla} \times \mathbf{B} = \frac{4\pi}{c}\mathbf{J}. \tag{2.2.17}$$

This implies a one-to-one relation between the current density **J** and the magnetic field **B**. Using this result and combining Eqs. (2.2.11) and (2.2.17), the electric field can be solved as

$$\mathbf{E} = \frac{c}{4\pi\sigma}\boldsymbol{\nabla} \times \mathbf{B} - \frac{\mathbf{v}}{c} \times \mathbf{B}. \tag{2.2.18}$$

This means that the electric field does not need to be treated as an independent variable in MHD, since it can be fully determined from the velocity field and the magnetic field. The induction equation is then obtained by substituting this result into *Faraday's law*,

$$\begin{aligned} \frac{\partial \mathbf{B}}{\partial t} &= -c\boldsymbol{\nabla} \times \mathbf{E} && (2.2.19) \\ &= \boldsymbol{\nabla} \times \left(-\frac{c^2}{4\pi\sigma}\boldsymbol{\nabla} \times \mathbf{B} + \mathbf{v} \times \mathbf{B} \right). && (2.2.20) \end{aligned}$$

Finally, introducing the magnetic diffusivity $\eta = c^2/4\pi\sigma$ and using the vector identity $\boldsymbol{\nabla} \times (\boldsymbol{\nabla} \times \mathbf{B}) = \boldsymbol{\nabla}(\boldsymbol{\nabla} \cdot \mathbf{B}) - \nabla^2\mathbf{B}$, together with the solenoidal condition $\boldsymbol{\nabla} \cdot \mathbf{B} = 0$, one obtains

$$\frac{\partial \mathbf{B}}{\partial t} = \boldsymbol{\nabla} \times (\mathbf{v} \times \mathbf{B}) + \eta\nabla^2\mathbf{B}. \tag{2.2.21}$$

2.2.3 Theories behind strong magnetic fields

The origin of strong, organized magnetic fields observed in Ap stars has long been a subject of debate, leading to the development of two main theoretical scenarios: the core-dynamo theory and the fossil-field theory. In the core-dynamo framework, magnetic fields are generated by dynamo action in the convective core and subsequently transported into the surrounding radiative envelope. However, this mechanism faces several difficulties and the challenge of reproducing the predominantly large-scale magnetic geometries inferred from observations.

The fossil-field theory provides an alternative explanation, in which the observed magnetic fields are relics of earlier evolutionary stages and persist within the radiative interior of the star. This framework naturally accounts for the large-scale structure, long-term stability, and wide range of field strengths observed in strongly magnetized stars, making it the favored explanation for the magnetic properties of Ap stars.

2.2.3.1 Fossil field theory

Since the pioneering calculations made by Cowling (1945), we know that large-scale magnetic fields could persist in radiative stars for considerably longer than their MS lifetimes. This longevity suggests a possible primordial origin, consistent with the hypothesis of fossil magnetic fields (e.g. Braithwaite and Spruit, 2017; Schleicher et al., 2023). In this case, the magnetic fields must have survived the pre-main-sequence phase of stellar evolution, which at least preferentially is more feasible when the protostars are radiative as well.

According to the MHD equations, the magnetic field $\mathbf{B}$ evolves as described by the induction equation (2.2.21), while the fluid velocity evolves according to the momentum equation (2.2.2). In an unmagnetised star in hydrostatic equilibrium, the pressure gradient balances gravity, resulting in a stationary configuration. However, in a magnetized star, a stable equilibrium is reached when the pressure gradient, gravity, and the Lorentz force are in balance.

In analogy with the analysis of the static case of the stellar structure equations, which leads to hydrostatic equilibrium, one may also investigate static solutions of the MHD equations. In this context, a static configuration corresponds to the absence of bulk motion, so that the velocity field vanishes, $\mathbf{v} = \vec{0}$. Substituting this condition into the momentum equation yields

$$-\rho(\mathbf{v} \cdot \nabla)\mathbf{v} - \nabla P + \mathbf{j} \times \mathbf{B} + \mathbf{F}_g + \mathbf{F}_v = 0 \tag{2.2.22}$$

which expresses the balance between pressure, gravitational, viscous, and magnetic forces. The study of solutions satisfying this condition is known as magnetohydrostatic equilibrium. It is important to note, however, that a magnetic field **B** fulfilling this force balance does not necessarily correspond to a static solution of the induction equation.

In such a case, the system can settle in a static configuration also needs to be stable, allowing the possible survival of a **fossil magnetic field** (Braithwaite and Spruit, 2017). Bearing that in mind, the induction equation reduces to

$$\frac{\partial \mathbf{B}}{\partial t} = \eta \nabla^2 \mathbf{B}. \tag{2.2.23}$$

The fossil field hypothesis was first proposed by Cowling (1945), who showed that due to the resistive (or Ohmic) decay time, magnetic fields in radiative stars can survive for durations longer than their main-sequence (hereafter MS) lifetimes. In the case of the Sun, Cowling realized that the Ohmic diffusion time in radiative zones is around 10^{10} years. This decay timescale is approximately given by $\sim R^2/\eta$, where R is the stellar radius and η is the magnetic diffusivity. Cowling concluded that stellar magnetic fields could be remnants of magnetic fields of the primordial protostellar cloud from which they formed (Cowling, 1945; Dudorov and Khaibrakhmanov, 2015). Therefore, a magnetic field could survive the whole MS if it is in a stable equilibrium inside a radiative zone. Some of these stable configurations have already been simulated inside fully radiative A-type stars (Braithwaite and Spruit, 2004; Braithwaite and Nordlund, 2006; Braithwaite, 2008; Becerra et al., 2022).

However, as shown in Fig. (2.2.1), the survival of fossil fields is strongly dependent on the internal structure of the star. Stars with a purely convective protostellar evolution can almost completely dissipate the initial magnetic flux because of the turbulent motion. In contrast, if the interior is fully radiative or if the fossil field is strong enough to suppress the convection in the core, it may survive for a much longer time, comparable to the lifetime of the star (Moss, 1989; Schleicher et al., 2023).

The transition from a convective to a radiative phase in the protostellar structure is extremely relevant for the survival of these primordial magnetic fields and could help to preserve a significant part of the initial magnetic flux of the protostellar cloud, as envisioned by Dudorov and Tutukov (1990). The first detailed protostellar

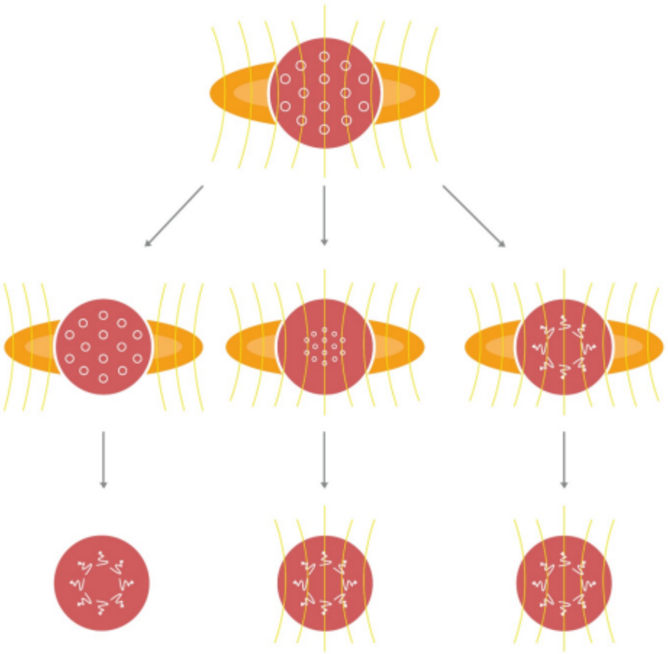

Figure 2.2.1: The orange color indicates the protostellar disk and yellow lines show the magnetic field. Circles indicate convective regions within the protostars, arrows represent radiative regions (Schleicher et al., 2023)

models for the intermediate mass that showed such a transition were proposed by Palla and Stahler (1990, 1991, 1992).

2.2.3.2 Core-dynamo fields theory

The core dynamo theory, on the other hand, is an alternative explanation which proposes that a dynamo mechanism operates within the stellar convective core and continuously regenerates the magnetic field that then is transported into the overlaying radiative layers, under the action of buoyancy, towards the surface (Braithwaite and Spruit, 2017). Specifically, in early-type stars, the formation of this convective core is driven by the temperature sensitivity to the CNO cycle. Under these conditions, convective motions and differential rotation can produce shear instabilities that can potentially generate strong magnetic fields through dynamo processes (Browning et al., 2004; Brun et al., 2005). According to estimations made by Lecoanet et al. (2022), a convective core dynamo could generate strong magnetic fields inside a B-type star, with an upper limit of $B_r \approx 500$ kG to its strength, exceeding what is possible to reach via fossil fields alone. Nevertheless, the existence of such a dynamo does not guarantee that the magnetic field will reach the stellar surface, forming coherent large-scale structures (MacDonald and Mullan, 2004), as only a fraction of the magnetic flux is effectively transported outward MacGregor and Cassinelli (2003); Hidalgo et al. (2024). There is also the possibility of interaction between this primordial field and the one generated by the core dynamo. In fact, Featherstone et al. (2009) modeled the coupling of a fossil field and a convective core dynamo within an A-type star, demonstrating that this interaction could produce a magnetic field strong enough to be transported to the surface by magnetic buoyancy, enhancing the action of the dynamo (MacDonald and Mullan, 2004). The impact of this interaction on the fossil magnetic field, both at the surface and within the radiative envelope, was recently investigated by Hidalgo et al. (2025), who found that certain configurations can enhance the core dynamo and lead to stable surface fields.

2.3 Limitations of the theoretical framework

The following section is based on the lectures notes of Warrick Ball.

At the beginning of Section (2.1), the general assumptions behind the theory of stellar structure were explained along with their consequences. However, there are certain limitations that must be kept in mind when these approximations are made. For instance, the fluid approximation breaks down when different particle species decouple, which occurs above the photosphere. Neglecting rotation is a more delicate assumption, since most stars do rotate, often at different rates, but rotation does not always lead to a significant modification of stellar structure. However, rotation introduces an important consequence, which is the additional mixing produced by fluid instabilities. This rotationally induced mixing can be relevant even when the structural effects of rotation themselves remain small. It is also known that many stars, including the Sun, have magnetic fields. These fields are present but usually not strong enough to play a dominant role in determining the global stellar structure. Lastly, local thermodynamic equilibrium becomes invalid near the stellar surface, where the radiation field deviates from the Planck function due to the formation of spectral lines in the low density atmospheric layers.

In Section (2.1.18), it is important to note that the main assumptions underlying the derivation of the radiative flux equations are that the photon mean free path must be much smaller than the stellar radius, that is, $\ell_{ph} \ll R$, and that the diffusion approximation is only valid when the medium is optically thick. Otherwise, one must solve the full radiative transfer equations.

In Section (2.1.2), the phenomenon of convection and the *mixing-length theory* are introduced; however, a complete theory of convection has not yet been formulated. Although the structure of intermediate-mass MS stars appears to be relatively well understood, several limitations remain within the approximations of current theoretical frameworks. In the case of the already mentioned MLT, which is widely used in stellar models, many assumptions must be introduced because it is fundamentally a simple theory. MLT is completely local, meaning that it considers only the local properties of the fluid such as temperature, density and their gradients. As a consequence, it neglects the inertia of an accelerating fluid parcel, which allows situations in which the acceleration becomes zero at the convective boundary, but the convective velocity remains finite when approaching this limit. In this situation, the fluid may penetrate into convectively stable regions, a process known as convective core overshooting. In MLT this is treated by introducing an additional free parameter, the overshooting parameter α_{ov}, which can be implemented in different ways, for instance as an exponential formulation, a step function, or through a diffusive approach. Since MLT cannot predict the extent of overshooting into stable layers, the prescriptions used to model it are considered ad hoc parametrizations. These parametrizations must be calibrated using observations, in the same way that the parameter α_{MLT} cannot be obtained from first principles. Another limitation is that there are several slightly different versions of MLT, which incorporate minor changes in the way convective flux is predicted and which may depend on opacity, blob geometry and other physical choices. Finally, a natural question arises, regarding why MLT has persisted for so long and how it manages to work at all. Although its simplifications may appear to be serious drawbacks for stellar modeling, MLT remains attractive because it is relatively easy to implement, computationally efficient and drives the temperature gradient close to its adiabatic value. Nevertheless, it fails near the surface of Sun-like stars, where convection becomes inefficient.

For completeness, it should be noted that several alternative convection theories have been developed, although MLT remains the most widely used. One of them is the so-called full-spectrum theory (FST), which relies on the full range of turbulent eddies and was formulated by Canuto and Mazzitelli (1991, 1992) and Canuto et al. (1996). Another family of approaches, more advanced than MLT, corresponds to non-local and time-dependent convection theories. A generalized analytical extension of MLT was proposed by Gough and Weiss (1976); Gough (1977), while an alternative formulation derived from hydrodynamic equations and turbulence modeling was developed by Xiong (1978, 1980, 2021). further discussion of these alternative theories is not pursued in this work.

Chapter 3

Numerical method

For the sake of obtaining realistic solutions to the equations, one has to rely on numerical integration of the differential system. At the time Schwarzschild was working on stellar evolution models, astronomers still had to carry out numerical calculations by hand, and as remarked by Schwarzschild (1958), “A person can perform more than twenty integration steps per day", so that "for a typical single integration consisting of, say, forty steps, less than two days are needed” Kippenhahn et al. (2012). However, with the advent of large and fast electronic computers, the pace accelerated enormously.

Today, the situation has changed drastically, as numerous stellar evolution codes have been developed to address a broad range of astrophysical problems, producing numerical and physical solutions far more refined than those obtained fifty years ago. These tools now enable detailed modeling across a wide spectrum of stellar masses and evolutionary phases. Notable examples include the Geneva code (Ekström, S. et al., 2012; Georgy et al., 2013), STARS (Eggleton, 1971; Pols et al., 1995), STERN (Brott et al., 2011), the Padova/PARSEC models (Girardi et al., 2002; Bressan et al., 2012) and, of course, the `MESA` code Paxton et al. (2011, 2013, 2015, 2019); Jermyn et al. (2023). Together with the growing availability of precise tabulated opacities, nuclear reaction rates, and equations of state, the resulting developments have also facilitated major advances in stellar astrophysics (Choi et al., 2016). Therefore,in order to simulate the protostellar evolution considering different accretion scenarios, we employ the `MESA` stellar evolution code to solve the fundamental stellar structure equations, which allows us to analyze the internal structure and evolution of the star by identifying the transition from a convective to a radiative regime.

3.1 Introduction

Analytic solutions to the differential equations governing stellar structure and evolution are not possible for realistic physical conditions, making numerical methods essential. The naive approach is the *shooting method*. Analogous to adjusting a cannon's aim through trial and error, this technique involves guessing the central values of pressure and temperature, given the star's mass and composition, and integrating the stellar structure equations outward from the center to the surface. The goal is to hit the prescribed surface boundary conditions, such as effective temperature and pressure, in a single forward integration from the core.

In practice, however, this method suffers from severe numerical instability. The stellar structure equations are inherently sensitive to the initial conditions, such that minute errors in the guessed central values are exponentially amplified during the outward integration. This behavior is particularly pronounced in the radiative transport equation (2.1.18), where the temperature dependence enters through a factor proportional to T^{-4} , greatly enhancing the sensitivity of the solution. As a consequence, small mismatches at the center typically lead to large deviations near the stellar surface, making it extremely difficult to satisfy the surface pressure and temperature boundary conditions simultaneously. This high sensitivity renders the shooting method inefficient and impractical for realistic and complex stellar models. Nevertheless, this fundamental limitation was overcome with the introduction of the method developed by Henyey et al. (1964), who introduced an efficient technique to calculate stellar models in hydrostatic equilibrium. This approach has since become standard in the field, and the `MESA` code implements a Henyey style scheme with additional numerical refinements to solve the stellar structure equations efficiently and robustly.

3.2 The `MESA` code

The open-source one-dimensional stellar evolution code `MESA` (version r23.05.1; Paxton et al. 2011, 2013, 2015, 2019; Jermyn et al. 2023) computes models of spherically symmetric single stars. `MESA` is a highly modular framework designed to simulate a wide variety of stellar evolution scenarios. Its main engine is the `MESA star` module, which constructs one-dimensional, spherically symmetric stellar models by combining a set of numerical and physical modules. These models can describe stellar evolution over a broad range of initial masses, from low-mass to massive stars.

The `MESA star` module solves the fully coupled Lagrangian equations of stellar structure and chemical composition simultaneously, using the enclosed mass coordinate M_r as the independent variable. At each time step, it coordinates the interaction with additional modules that provide the required microphysical inputs, such as the equation of state, opacities, nuclear reaction rates, nuclear reaction networks, and element diffusion coefficients. Each of these components is implemented as an independent public library written in `Fortran 95`, facilitating both code maintenance and user development.

From a numerical perspective, the stellar structure is discretized into a finite number of zones, typically ranging from several hundred to several thousand, depending on the evolutionary stage and the physical complexity of the model. These zones are indexed from the stellar surface inward toward the center. `MESA` adopts a finite volume formulation and flux conservation, which implies dividing the star into cells of finite volume and ensuring that mass and energy are conserved across cell interfaces. Within this discretization scheme, each zone is associated with a cell and an outer face, and the `MESA star` module solves the fully coupled system of equations for all zones simultaneously using a Newton–Raphson method implemented in a dedicated numerical solver. As shown in Fig. (3.2.1), mass-averaged quantities, such as density ρ_k, temperature T_k, and the vector of mass fractions $X_{i,k}$, are defined in the cell centers and represent the local thermodynamic and compositional properties averaged by mass of the stellar material of that volume. Boundary variables, on the other hand, including enclosed mass m_k, radius r_k, luminosity L_k, and velocity v_k, are defined on the outer faces of cells and describe their geometric location and the fluxes that cross each zone.

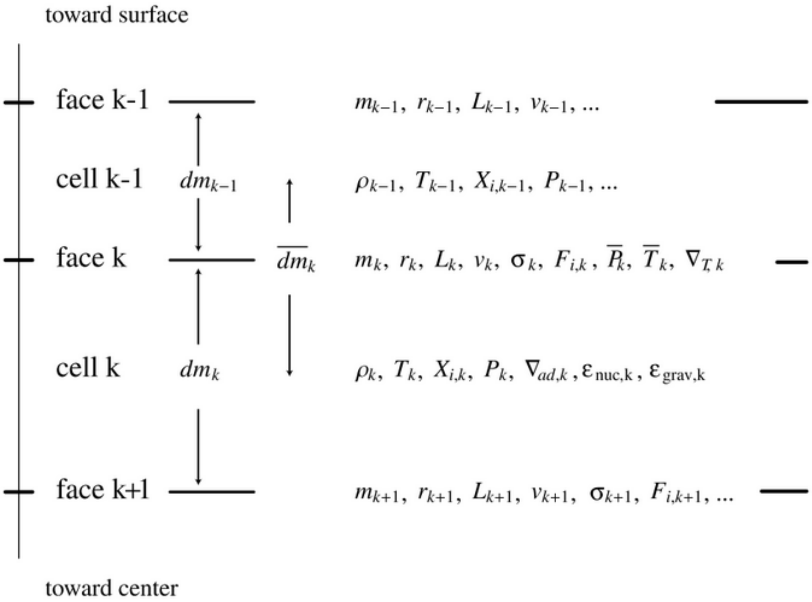

Figure 3.2.1: Schematic of the discretization process showing some cell and face variables.

For the sake of numerical stability of the linear system, the original equations are discretized and reformulated to ensure a finite volume formulation. The **continuity equation** (2.1.1), which enforces mass conservation, is integrated between the radii r_k and r_{k+1}. In `MESA star` , grid indices increase toward the stellar center, such that $r_k > r_{k+1}$. The resulting expression is then algebraically rearranged to improve numerical stability[1] and to minimize round-off errors, yielding

$$\rho_k = \frac{dm_k}{\frac{4}{3}\pi\left(r_k^3 - r_{k+1}^3\right)} \tag{3.2.1}$$

$$\iff \quad \ln r_k = \frac{1}{3}\ln\left[r_{k+1}^3 + \frac{3}{4\pi}\frac{dm_k}{\rho_k}\right]. \tag{3.2.2}$$

The momentum conservation equation (2.1.2) sets the pressure P_k at interior cell boundaries (cell faces), where $\overline{dm}_k = 0.5\,(dm_{k-1} + dm_k)$ and a_k is the Lagrangian acceleration evaluated at face k. For numerical stability, the equation is rescaled by $\overline{P}_k = (P_{k-1}dm_k + P_k dm_{k-1})/(dm_k + dm_{k-1})$, which is the pressure interpolated

---

[1] This equation is additionally rescaled by the local sound speed to enhance numerical stability.

by mass at face k, yielding

$$\begin{aligned} \frac{P_{k-1} - P_k}{\overline{P}_k} &= \frac{\overline{dm_k}}{\overline{P}_k} \left[-\frac{G m_k}{4\pi r_k^4} - \frac{a_k}{4\pi r_k^2} \right] && (3.2.3) \\ &= \frac{\overline{dm_k}}{\overline{P}_k} \left[\left(\frac{dP}{dm} \right)_{\text{hydrostatic}} + \left(\frac{dP}{dm} \right)_{\text{hydrodynamic}} \right] && (3.2.4) \end{aligned}$$

where the hydrodynamic part is set to zero in case of hydrostatic equilibrium, because of the acceleration term $a_k = 0$.

The energy transport equation (2.1.4) determines the temperature difference across interior cell boundaries, thereby setting the temperature of interior cells T_k. For numerical stability, the equation is rescaled by $\overline{T}_k = (T_{k-1} dm_k + T_k dm_{k-1})/(dm_k + dm_{k-1})$, which is the temperature interpolated by mass at face k, yielding the discretized form

$$\frac{T_{k-1} - T_k}{\overline{T}_k} = \overline{dm_k} \left[\nabla_{T,k} \left(\frac{dP}{dm} \right)_{\text{hydrostatic}} \frac{1}{\overline{P}_k} \right], \qquad (3.2.5)$$

where $\nabla_{T,k} = d \ln T / d \ln P$ is evaluated at face k.

The energy conservation equation (2.1.3) for cell k is written as

$$L_k - L_{k+1} = dm_k \left(\epsilon_{\text{nuc}} - \epsilon_{\nu,\text{thermal}} + \epsilon_{\text{grav}} \right). \qquad (3.2.6)$$

The evolution of the mass fraction $X_{i,k}$ of species i in cell k is governed by the composition equation (2.1.5), which in finite-volume form becomes

$$\begin{aligned} X_{i,k}(t + \delta t) - X_{i,k}(t) &= dX_{\text{burn}} + dX_{\text{mix}} \\ &= \frac{dX_{i,k}}{dt} \delta t + (F_{i,k+1} - F_{i,k}) \frac{\delta t}{dm_k}, && (3.2.7) \end{aligned}$$

where $dX_{i,k}/dt$ is the rate of change due to nuclear reactions and $F_{i,k}$ is the mass flux of species i across face k.

The compositional flux, or the mass of species i flowing across a face k,is given by

$$F_{i,k} = (X_{i,k} - X_{i,k-1}) \frac{\sigma_k}{dm_k}, \qquad (3.2.8)$$

where σ_k is the Lagrangian diffusion coefficient evaluated at face k.

The reformulated stellar structure equations (3.2.2), (3.2.3), (3.2.5), (3.2.6), and (3.2.8), as described in Paxton et al. (2011), are solved simultaneously in a fully coupled manner using a first-order backward differencing time integration scheme.

3.3 Adopted physics and input parameters

In order to compute stellar evolutionary models, it is necessary to specify the physical ingredients included in the calculations. Within `MESA` , a wide range of physical options and parameters can be selected to control the level of complexity of the models, and the code can also be modified to include additional prescriptions not available by default. These choices are specified through the INLIST files, where the relevant physical assumptions and numerical parameters are defined.

In this study, we compute protostellar evolution models with an initial mass of one solar mass for all cases, adopting different metallicities of $Z = 0.001$, 0.01, 0.02, and 0.03. We adopt a fixed mixing-length parameter of $\alpha_{\rm MLT} = 1.82$, following Choi et al. (2016), which is close to the solar-calibrated value and parametrizes the efficiency of convective energy transport. Convection is treated using the modified mixing-length theory of Henyey et al. (1965), which accounts for radiative losses from convective elements.

Convective overshooting is included using an overshoot parameter of $f_{\rm ov} = 0.016$, following Choi et al. (2016). This parameter sets the extent of the overshoot region beyond the convective boundary defined by the Schwarzschild criterion (see Eq. (9) of Paxton et al. (2013)). Although overshooting has little impact during the earliest phases of protostellar evolution, it can become relevant at later stages, particularly once a convective core develops.

For the equation of state and opacities, we adopt the default `MESA` configuration. The equation of state is primarily based on the OPAL and SCVH tables (Rogers and Nayfonov, 2002; Saumon et al., 1995). Radiative opacities are taken from the high-temperature tables of Grevesse and Sauval (1998) and the low-temperature tables of Ferguson et al. (2005). Electron conduction opacities are computed following the prescription of Blouin et al. (2020).

The modular structure of `MESA` allows us to easily explore different physical prescriptions within the simulations and to implement new physics in a straightforward manner. For the simulations presented here, we implemented a module that prescribes a time-dependent accretion rate, defined through a chosen functional form. This framework naturally includes the constant accretion-rate case. The corresponding code is provided in Appendix A5.2.

For the accreted material, we assume that the composition is identical to that of the current stellar surface and, consequently, that the entropy of the accreted material matches the entropy of the stellar surface prior to accretion. This corresponds to the assumption of *cold disk accretion* (Palla and Stahler, 1992; Hosokawa et al., 2010; Haemmerlé et al., 2013), which means that matter is gently deposited onto the stellar surface. In this way, we will consider constant rates as well as time-dependent accretion rates, including a power-law decrease and time-dependent fluctuations, as outlined below.

All models studied here are evolved until they reach the ZAMS, using the stopping condition `stop_near_ZAMS`. This phase begins when nuclear fusion within the protostar becomes the dominant source of energy. In `MESA` it is defined as $L_{\rm nuc}/L > 0.9$, that is, when most of its luminosity begins to come from nuclear fusion.

Regions that appear convectively unstable under the Schwarzschild criterion (hereafter SCHC) can actually be stable when composition gradients are taken into account. This condition defines what is known as semiconvection, which is included in the code by specifying the use of the Ledoux criterion to treat convection in simulations. However, for this project, the SCHC is sufficient to quantify the transition between radiative and convective phases, since composition gradients are not significant for a single star at the beginning.

3.4 Criteria to quantify the transition

To analyze the internal structure of the protostars, we use the Kippenhahn diagrams, similar to Palla and Stahler (1991, 1992), also called space-time diagrams, to illustrate the evolution of the protostellar interior and to determine the convective and radiative regions. The main equation that `MESA` has to solve in order to obtain the necessary data is equation (2.1.4), through which the gradient will be obtained from the following conditions:

$$\nabla = \begin{cases} \nabla_{\rm rad} = \frac{3\kappa}{16\pi acG}\frac{L_r P}{M_r T^4}, & \text{if } \nabla_{\rm rad} \leq \nabla_{\rm ad} \\ \nabla_{\rm ad} + \Delta\nabla, & \text{if } \nabla_{\rm rad} > \nabla_{\rm ad} \end{cases} \tag{3.4.1}$$

where ∇_{rad} and ∇_{ad} are the radiative and adiabatic temperature gradients, respectively, and $\Delta\nabla$ refers to the superadiabatic excess[1] in a convective region. The variables κ, a, G and c denote the opacity, the radiation constant, the gravitational constant and the speed of light, respectively. This equation defines the temperature gradient ∇ inside the star and takes two possible forms depending on whether the radiative gradient $\nabla_{\rm rad}$ is less than or equal to the adiabatic gradient $\nabla_{\rm ad}$. If $\nabla_{\rm rad} < \nabla_{\rm ad}$, the energy is transported by radiation and ∇ equals $\nabla_{\rm rad}$, which is given by the expression above. If $\nabla_{\rm rad} > \nabla_{\rm ad}$, convection sets in and the gradient is $\nabla_{\rm ad} + \Delta\nabla$. Therefore, on the basis of the temperature gradients and applying the SCHC, we can distinguish between radiative and convective regions within the protostar.

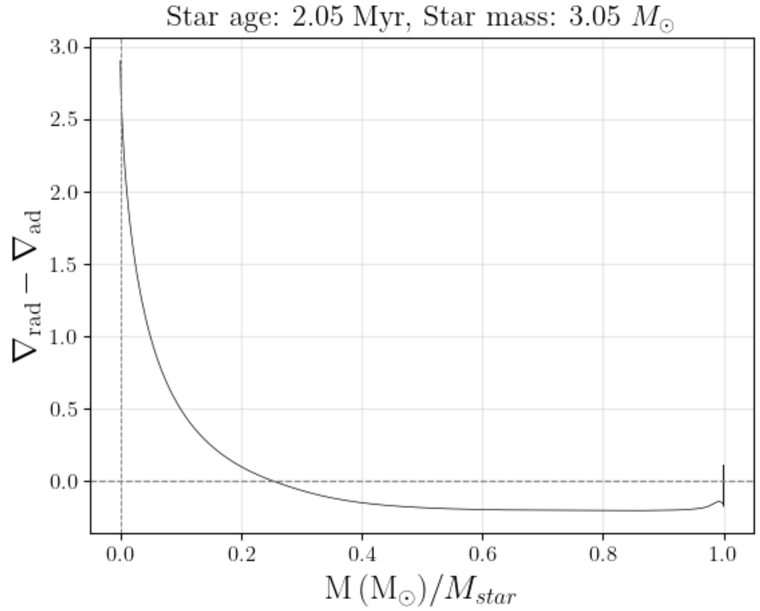

Figure 3.4.1: Protostar of 2.05 Myr shows convection at roughly 23% of the normalized mass.

The quantity $\nabla_{\rm rad} - \nabla_{\rm ad}$, known as the superadiabaticity, allows us to determine

---

[1] This is the correction applied when convection is not perfectly adiabatic.

the relative importance of radiative and convective energy transport within the protostar. Figure (3.4.1) shows a model of a protostar with an initial mass of 1 $M_\odot$ at an age of 2.05 Myr. An analysis of the superadiabaticity reveals regions where this difference is positive and others where it is negative. These regions correspond to convectively unstable and radiatively stable layers, respectively. From this profile, we find that the stellar interior is composed of approximately 23% convective regions and 77% radiative regions at this evolutionary stage.

We define the structural transition point as the stage at which 50% of the stellar interior becomes radiative. The corresponding stellar mass at this stage is defined as the transition mass, M_{tr}.

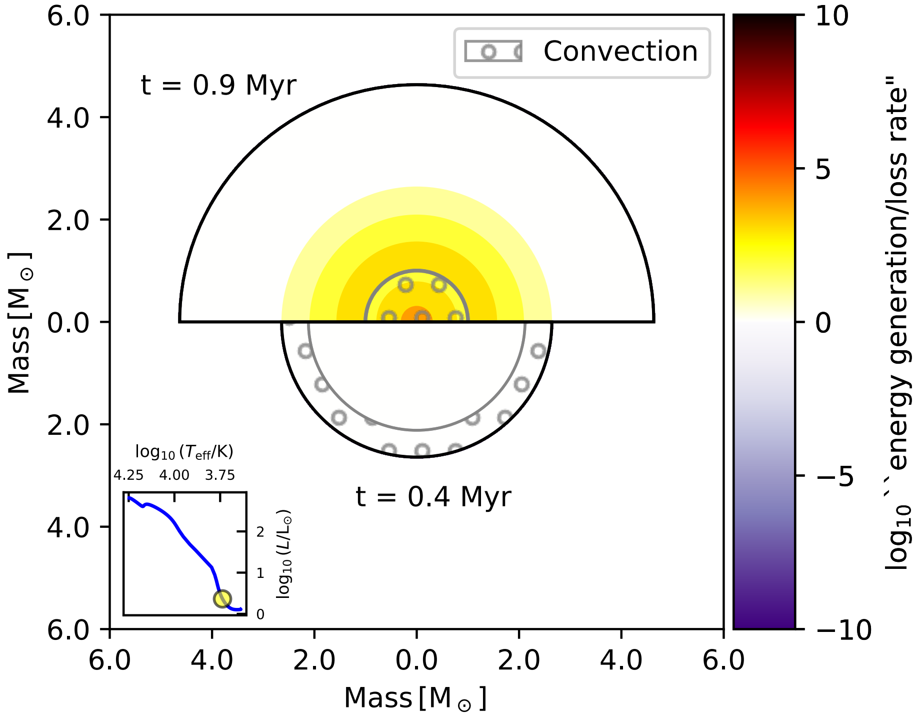

Figure 3.4.2: Diagram showing the internal structure of a star, produced using the TULIPS code (Laplace, 2022). This diagram is equivalent to a Kippenhahn diagram. Convective transport is shown with circles. It displays two evolutionary stages of the same star: an early stage at an age of 0.4 Myr and a later stage at 0.9 Myr, in which the star has developed a radiative envelope and has accreted more mass. Star mass is shown on both axes.

Figure (3.4.2) shows the internal structure of one of the stellar models evolved in this project. The model parameters are listed in Table (A1.1), corresponding to the case with an accretion rate of $\dot{M} = 3.98 \times 10^{-6}\,\mathrm{M}_{\odot}\,\mathrm{yr}^{-1}$. The figure illustrates the temporal evolution of the same star and highlights the development of a convective core at later stages of its evolution. The star is initially fully convective, but it rapidly develops a radiative core, while the convective envelope progressively becomes thinner with time. Using the superadiabaticity, it becomes straightforward to determine whether a given region is radiative or convective, which in turn allows us to compute the corresponding fractions of the stellar interior.

In some cases, there were multiple locations where the superadiabaticity crossed zero. As a result, the stellar interior could contain several disconnected radiative regions, forming isolated "islands" embedded within convective zones, as illustrated in Fig. 3.4.3. In such situations, the radiative fraction cannot be determined by identifying a single transition point, since no unique boundary exists between radiative and convective regions.

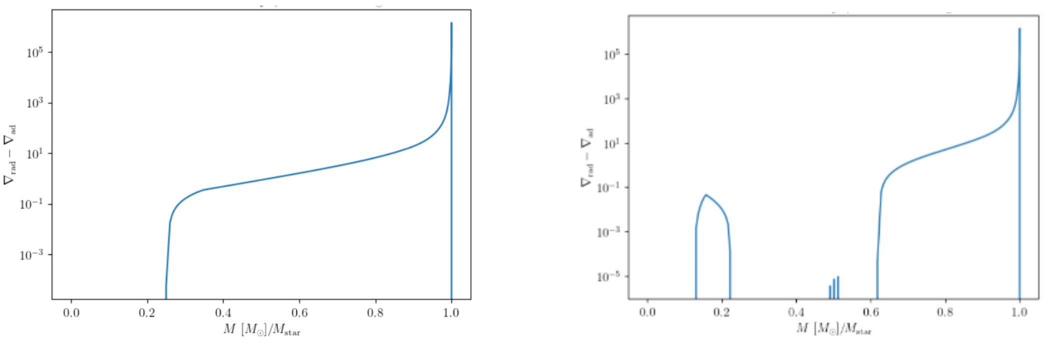

(a) Superadiabaticity profile showing one boundary between radiative and convective transport.

(b) Superadiabaticity profile with multiple boundaries.

Figure 3.4.3: Examples of superadiabaticity profiles. In some cases, multiple zero crossings appear.

To address this, we adopt a more general approach based on the mass distribution of the stellar interior. The stellar structure is divided into mass shells, and only those shells in which radiative transport is active are selected. By summing the masses of all radiative shells, the total radiative mass fraction can be computed. The following code illustrates how these percentages were calculated in the general case.

```
def radiative_percentage(mass, grada, gradr):
    if not np.all(np.diff(mass) > 0):
        sort_idx = np.argsort(mass)
        mass = mass[sort_idx]
        grada = grada[sort_idx]
        gradr = gradr[sort_idx]

    delta_grad = gradr - grada
    is_radiative = delta_grad < 0

    dm = np.diff(mass, prepend=mass[0])
    masa_total = np.sum(dm)
    masa_radiativa = np.sum(dm[is_radiative])
    porcentaje_radiativo = (masa_radiativa /
        masa_total) * 100

    mass_norm = mass / np.max(mass)
return porcentaje_radiativo, mass_norm, is_radiative
```

First, the function ensures that the mass array is monotonically increasing, meaning that it is ordered from the stellar center to the surface. This step is essential, as it guarantees that the mass differences between consecutive shells are well defined and positive. The superadiabaticity is then computed, and a boolean mask is constructed to identify radiative regions, defined by $\nabla_{\rm rad} - \nabla_{\rm ad} < 0$.

Next, the mass difference between consecutive shells is calculated as

$$\Delta m_i = m_i - m_{i-1}, \tag{3.4.2}$$

If the mass array were not monotonically increasing, this procedure would lead to negative values of Δm_i, yielding unphysical results.

The total mass contained in radiative regions is then obtained by summing the mass differences over all shells identified as radiative,

$$\sum_{\rm radiative} \Delta m_i. \tag{3.4.3}$$

Finally, the fraction of the stellar mass residing in radiative zones is computed by normalizing this quantity to the total stellar mass. This approach is both general and robust, as it remains valid regardless of the number of zero crossings of the superadiabaticity profile.

Throughout this work, this method is used to determine how the transition mass depends on metallicity and on the time-averaged accretion rate (see Eq. 4.2.2) during protostellar evolution, considering scenarios with time-dependent, fluctuating, and decreasing accretion rates.

Chapter 4

Simulations of protostellar structure

In this section, we present the results of the protostellar evolution for different accretion scenarios, including both constant and time-dependent accretion rates. Our main objective is to determine the transition mass at which at least half of the protostar becomes radiative. We examine how this transition mass depends on the average accretion rate, the metallicity, and the specific accretion scenario adopted. The MESA input files, including inlists, data files, and the source code used to reproduce the models and figures, are publicly available on Zenodo at doi:10.5281/zenodo.17652487.

4.1 Constant accretion rate

Our simplest scenario for accretion corresponds to a constant accretion rate $\dot{M}$ on the protostar. To illustrate and analyze the evolution of a protostar, a useful plot is the Kippenhahn diagram. In Figure (4.1.1) we show four examples for different cases of a constant accretion rate. The initial protostellar mass corresponds to 1 $\mathrm{M}_\odot$ and it is assumed to have solar metallicity (Z=0.02). We then explore accretion rates ranging from 10^{-6} to $1.5 \cdot 10^{-4}$ $\mathrm{M}_\odot/\mathrm{yr}$. In this diagram, the horizontal axis corresponds to the time and the vertical axis to the radial coordinate inside the star. The green-hatched area indicates the protostellar region, which is convective, while the white region is radiative. The blue color indicates the energy production within the protostar. The black solid line corresponds to the protostellar radius.

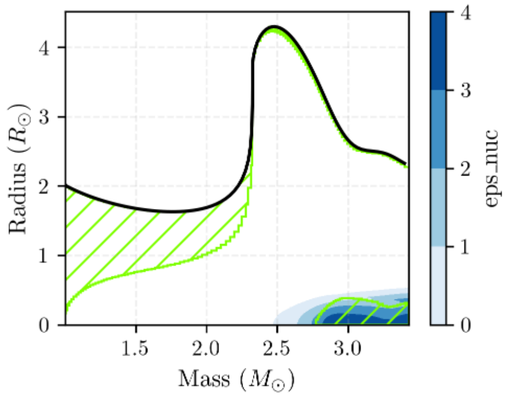

(a) $\dot{M} = 1.00 \cdot 10^{-6}$ M$_\odot$ yr^{-1} **(b)** $\dot{M} = 3.98 \cdot 10^{-6}$ M$_\odot$ yr^{-1}

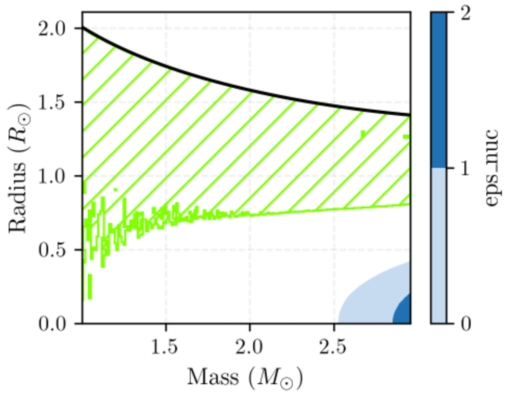

(c) $\dot{M} = 3.98 \cdot 10^{-5}$ M$_\odot$ yr^{-1} **(d)** $\dot{M} = 1.50 \cdot 10^{-4}$ M$_\odot$ yr^{-1}

Figure 4.1.1: Kippenhahn diagrams for four different constant accretion rates and a solar metallicity of $Z = 0.02$. We show four different models that assume different values of the constant accretion rate $\dot{M}$. The y-axis corresponds to the radial coordinate in the protostar, the x-axis denotes mass evolution. Green indicates the convective parts of the star, empty space indicates the radiative zones. The color bar represents the energy generation rate in the central core. All the models are evolved until ZAMS.

The top left panel in Figure (4.1.1) corresponds to the evolution with an accretion rate of $1.5 \cdot 10^{-6}$ M$_\odot$ yr^{-1}. In this case, the protostellar radius is initially around 2 R$_\odot$ and decreases a bit until it reaches one million years. Then, it increases steeply at 1.5 million years when energy production begins in the central core and reaches a final value of nearly 3 R$_\odot$ solar radii approaching the zero-age main sequence. At the beginning of the evolution, the protostar is mostly convective except for a small inner region; however, the radiative zone expands and the protostar is fully radiative after about 1.3 million years. The evolution is qualitatively similar in the top right panel corresponding to an accretion rate of $3.98 \cdot 10^{-6}$ M$_\odot$ yr^{-1}, though the corresponding timescales are shorter, as the protostellar radius rapidly expands at about 0.5 million years, which is also the time when it becomes fully radiative. In the case of a higher accretion rate ($3.98 \cdot 10^{-5}$ M$_\odot$ yr^{-1}) (bottom left panel), the behavior changes qualitatively as the radius initially increases as a result of accretion and it decreases steadily as a function of time as the accretion timescale $M/\dot{M}$ becomes longer compared to the Kelvin-Helmholtz timescale for contraction. In this case, the radiative zone of the protostar expands gradually over time, but it never becomes fully radiative. Even when the star reaches the zero-age main sequence, only about half of the star is radiative. The behavior is similar, but still more extreme for an accretion rate of $1.5 \cdot 10^{-4}$ M$_\odot$ yr^{-1} (bottom right panel). The Kippenhahn diagrams can be employed for analyzing where the transition to the radiative phase occurs (although for a more precise determination, we employed the superadiabaticity). If the transition is found to occur at a time $t_{\rm tr}$, the protostellar mass at that time is given as $M_{\rm tr} = 1$ M$_\odot + \dot{M} t_{\rm crit}$, where $\dot{M}$ is the accretion rate of the model. In this way, in Figures (4.1.1a) to (4.1.1d), the different accretion rates correspond to the transition masses M_{tr} of (a) 1.64 M$_\odot$, (b) 1.97 M$_\odot$, (c) 2.44 M$_\odot$, and (d) 2.53 M$_\odot$. We note that the transition mass slightly increases with the accretion rate, consistent with the results of Palla and Stahler (1991, 1992).

Our complete suite of simulations with constant accretion rates is summarized in Table (A1.1), and the corresponding Kippenhahn diagrams are shown in Figs. (A6.1)–(A6.4). In Figure (4.1.2), we present the transition mass obtained for 48 different simulations as a function of the accretion rate, for the absolute metallicities of $Z = 0.03, 0.02, 0.01, 0.001$. The shapes of the curves are qualitatively similar but quantitatively different. At first, the transition mass increases steeply with the accretion rate, while it then gradually flattens and increases more mildly at later stages. In general, the curves appear to be well described with the following equation: $M_{\rm tr} = a \log_{10}\langle \dot{M} \rangle + b$. The fits to the obtained results are provided in Table (A2.1), where we provide the parameters a and b for each metallicity. For the high metallicity case ($Z = 0.03$), the transition mass starts out at ~ 1.6 M$_\odot$for an accretion rate of $\sim 10^{-6}$ M$_\odot$ yr^{-1} and increases to ~ 2.7 M$_\odot$ for an accretion rate of $1.5 \cdot 10^{-4}$ M$_\odot$ yr^{-1}. The transition mass decreases with metallicity and for the lowest metallicity case with $Z = 0.001$, it starts at ~ 1.4 M$_\odot$ and reaches a final value close to 2 M$_\odot$.

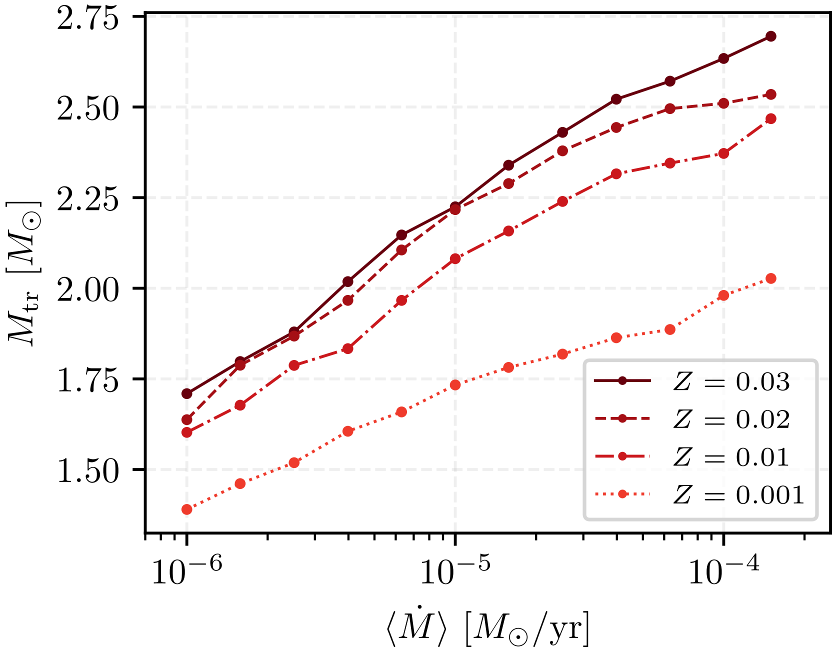

Figure 4.1.2: Results for the models with constant accretion rate. We show here the transition mass for which at least 50% of the protostar is radiative as a function of the average accretion rate as defined via Eq. 4.2.2, which here is equal to the constant accretion rate assumed in the model. The results are given for four different metallicities.

4.2 Fluctuating accretion rate

We introduce a fluctuating accretion rate that includes periodic variations. These could mimic episodic accretion events or instabilities in the circumstellar disk (e.g. Riaz et al., 2018, 2021). In this case, we assume that the accretion rate consists of a constant component, which we defined as $\dot{M}_0 = 10^{-6}$ M$_\odot$/yr, plus a fluctuating one. We model the fluctuating one as a positive contribution, via a square of the sine function, to allow for the peaks of accretion to significantly exceed the constant contribution. For this purpose, we vary the amplitude A and the characteristic period P. The time-dependent accretion rate is then given as

$$\dot{M}(t) = \dot{M}_0 + A\sin^2\left(\frac{t}{P}\right). \tag{4.2.1}$$

For a meaningful comparison with the results in the context of constant accretion rates, we introduce here the time-averaged accretion rate, which we can formally calculate as the difference between the initial and final mass divided by the time for accretion:

$$M_{av} = \langle M \rangle = \int_0^{t_{MS}} \frac{\dot{M}}{t_{total}} dt = (M_{final} - M_{initial}) \cdot \frac{1}{t_{total}}. \qquad (4.2.2)$$

4.2.0.1 Dependence on metallicity

We have modeled the fluctuating accretion rate for a period of $50,000$ years and a range of metallicities from 0.001 to 0.03. In Figure (4.2.1), all models for this setup are shown, and the complete data points are presented in Tables A4.3–A4.6. In this case, we note that, for lower metallicities, the plot appears to be the same as for the constant accretion rate scenario, starting from $M_{\rm crit} = 1.45$ M$_\odot$ at $Z = 0.001$, $M_{\rm crit} = 1.68$ M$_\odot$ at $Z = 0.01$, $M_{\rm crit} = 1.77$ M$_\odot$ at $Z = 0.02$ and $M_{\rm crit} = 1.80$ M$_\odot$ at $Z = 0.03$. As the metallicity increases, some differences appear, and between $Z = 0.02$ and $Z = 0.03$ a drop can be seen in the fluctuating accretion rate scenario, between $\langle \dot{M} \rangle = 5 \cdot 10^{-6} \;-\; 9 \cdot 10^{-6}$ [M$_\odot$/yr], in which the transition mass decreases from 2.07 to 1.98 solar masses for $Z = 0.02$ and from 2.12 to 1.99 solar masses for $Z = 0.03$. Then, both continue to grow, reaching a final value of 2.76 and 2.78 solar masses, for $Z = 0.02$ and $Z = 0.03$, respectively. However, we note that for the cases with the highest accretion rates, the timescale to reach the main sequence becomes comparable to the period of the variations, and consequently, the accretion rate does not vary significantly, This behavior is most evident in the last case.

We found that the drop occurs because the accretion rate at the time of the transition is lower than the mean value, leading to an earlier transition.

4.2.0.2 Dependence on the timescale of the variations

We explored how the timescale of the variations affects the obtained relation by adopting a constant metallicity $Z = 0.02$, adopting three different periods to explore the influence of these changes on the transition mass of the star.

In Figure (4.2.2) the data points from Tables A4.1 and A4.2 are shown. We note that the plot starts with a very similar transition mass for all three scenarios. We have $M_{\rm tr} = 1.77$ M$_\odot$ for $P = 50,000$ years, $M_{\rm tr} = 1.76$ M$_\odot$ for $P = 25,000$ years, and $M_{\rm tr} = 1.75$ M$_\odot$ for $P = 10,000$ years. As the models evolve, we observe a greater fluctuation between the accretion rates $4 \cdot 10^{-6}$ - $2 \cdot 10^{-5}$ [$\mathrm{M}_\odot$/yr]. However, for accretion rates of about 10^{-4} [$\mathrm{M}_\odot$/yr], the transition masses of the respective protostars are again quite similar, with $M_{\mathrm{tr}} = 2.76\ \mathrm{M}_\odot$ for $P = 50,000$ years, $M_{\mathrm{tr}} = 2.61\ \mathrm{M}_\odot$ for $P = 25,000$ years and $M_{\mathrm{tr}} = 2.74\ \mathrm{M}_\odot$ for $P = 10,000$ years. We therefore conclude that the time period of these variations, at least within the limits explored here, does not affect the relation very significantly. Small dips occur in the cases of periods of 25.000 years and 50.000 years, as the transition occurs at a time when the accretion rate is close to a minimum.

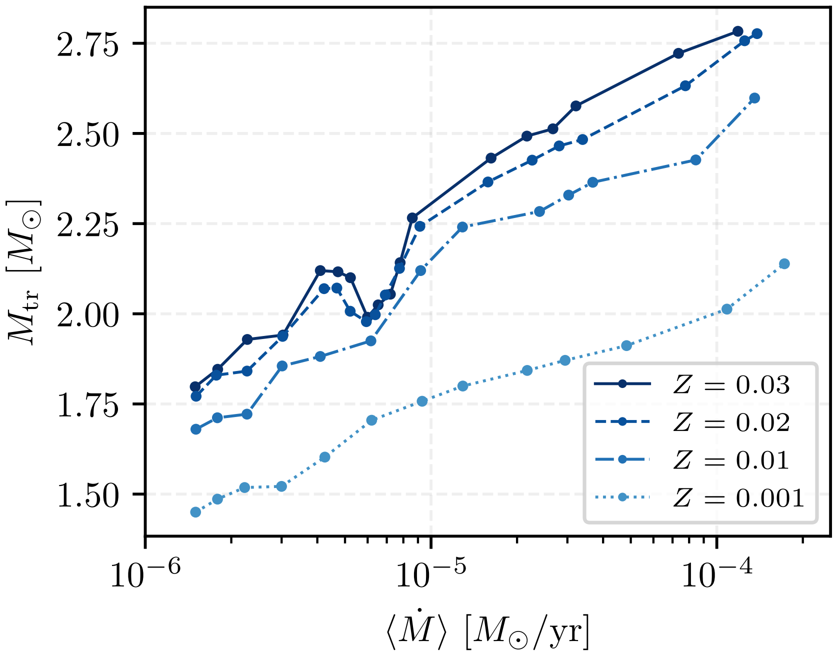

Figure 4.2.1: Results for the models with fluctuating accretion rate as defined in Eq. (4.2.1), assuming a fixed period of 50,000 years. We show here the transition mass for which at least 50% of the protostars is radiative as a function of the average accretion rate defined via Eq.(4.2.2). The results are given for four different metallicities ranging from 0.001 to 0.03.

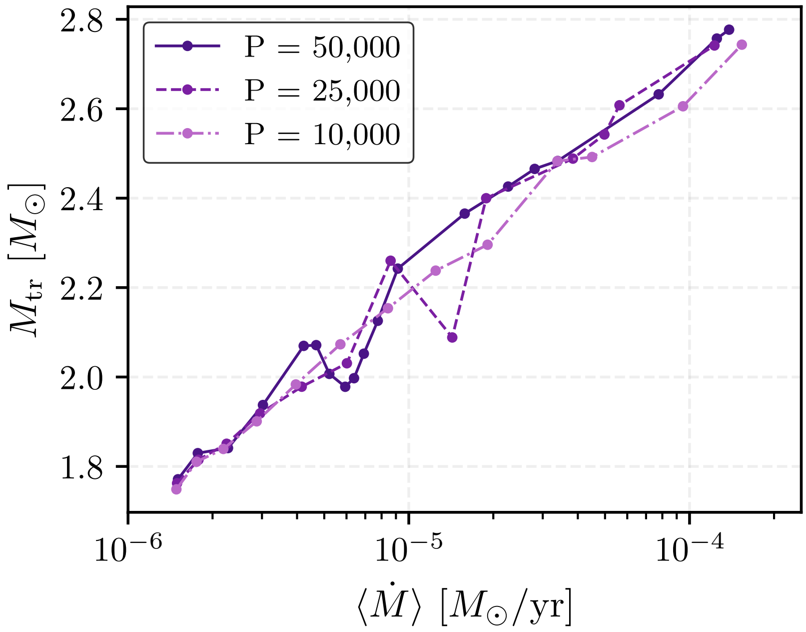

Figure 4.2.2: Results for the models with fluctuating accretion rates as defined in Eq. (4.2.1), assuming a constant metallicity of $Z = 0.02$. We show here the transition mass for the transition to the radiative state as a function of the average accretion rate defined via Eq.(4.2.2). The results are given for three different periods ranging from 10^4 years up to 5×10^4 years.

In Figure (4.2.3), we compare the results for a constant period and a constant metallicity. We observe that variations in the period of the fluctuation introduce more changes in the middle part of the plot, but the results remain almost identical for a given metallicity. In contrast, changes in the metallicity seem to be more relevant, as a clear dependence is observed.

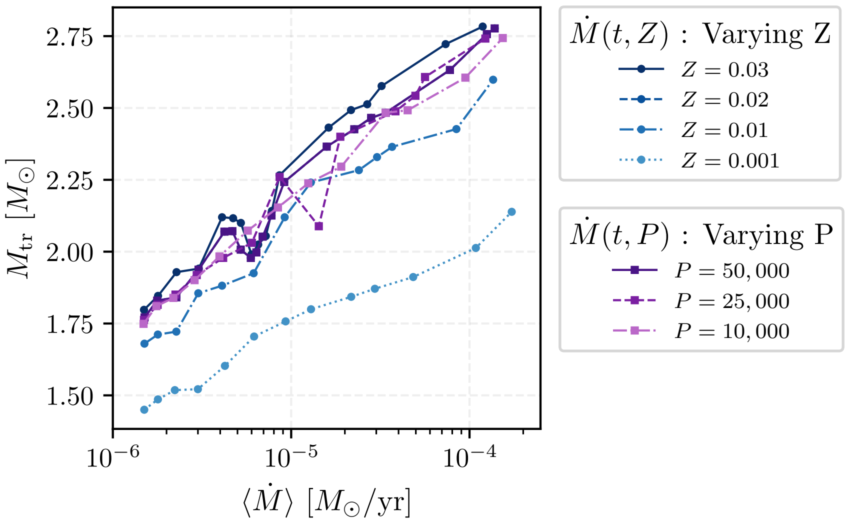

Figure 4.2.3: Comparison of models with different metallicities and models with different fluctuation periods. Blue corresponds to models where we have varied the metallicity, while purple corresponds to models where we varied the fluctuation period.

4.3 Power-law accretion rate

4.3.1 Power-law accretion rates

Finally, we introduce a new prescription that models a time-dependent accretion rate following a power-law behavior. This formulation aims to reproduce a scenario in which the accretion rate gradually decreases as the protostar evolves, reflecting the natural decline of material available in the surrounding envelope. Such a model provides a more realistic description of the late stages of protostellar growth compared to the constant or fluctuating cases. The adopted model can be written as

$$\dot{M} = \dot{M}_0 \left(\frac{t + t_0}{t_0} \right)^{\alpha}, \quad \text{with} \quad \alpha = -1, -2, -3. \tag{4.3.1}$$

The values for the initial accretion rate $\dot{M}_0$ range from 10^{-4} to 10^{-6} $\text{M}_\odot/\text{yr}$. The model starts with an initial mass of 1 $\text{M}_\odot$. Depending on the value of α, the characteristic time t_0 corresponds to the moment when the accretion rate drops to half its initial value ($\alpha = -1$), one-quarter ($\alpha = -2$) or one-eighth ($\alpha = -3$). In this context, t_0 acts as a reference for the time at which a significant decay in $\dot{M}$ is already observed, and this decay is faster for more negative α.

To explore the consequences of this prescription, we present again the transition mass as a function of the averaged accretion rate calculated from Eq. (4.2.2) for the different models.

4.3.1.1 Dependence on metallicity

We first consider models with a fixed decay exponent $\alpha = -1$ and explore the dependence on metallicity over the range $Z = 0.001$–0.03. Figure (4.3.1) shows the results corresponding to Tables A3.3–A3.6 for the different metallicities considered. The models located on the left-hand side of plot start with a transition mass of $M_{\rm tr} = 1.31,\ 1.43,\ 1.48,\ 1.49\ \mathrm{M}_\odot$ for $Z = 0.03, 0.02, 0.01, 0.001$, respectively.

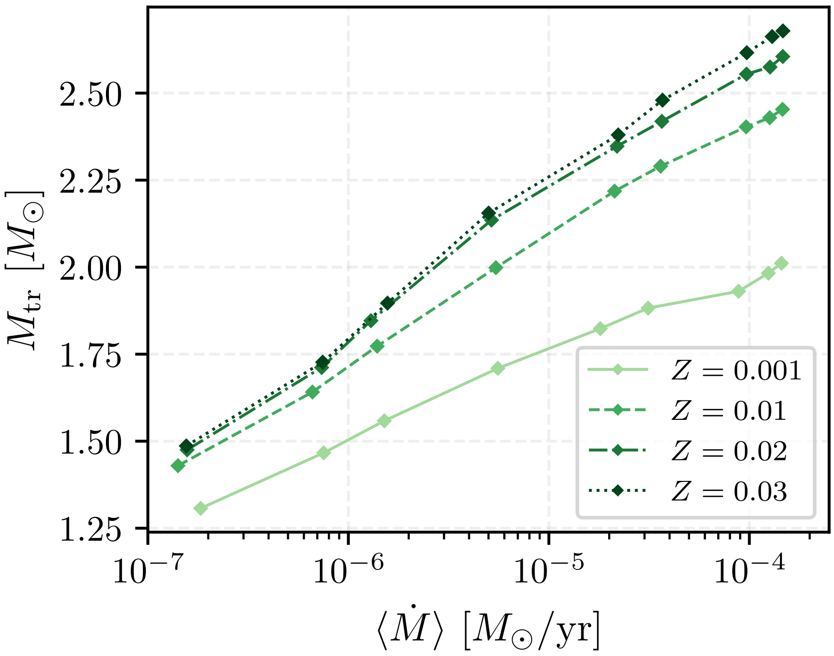

Figure 4.3.1: Results for the models with a power-law accretion rate, as defined in Eq. (4.3.1), assuming $t_0 = 300,000$ years and a power-law index of $\alpha = -1$. Here, we show the transition mass for which at least 50% of the protostars are convective as a function of the average accretion rate defined via Eq.(4.2.2). The results are given for four different metallicities.

For initial accretion rates of order $10^{-6}\,\mathrm{M}_\odot\,\mathrm{yr}^{-1}$, the time-averaged accretion rate decreases to values of order $10^{-7}\,\mathrm{M}_\odot\,\mathrm{yr}^{-1}$. As the average accretion rate increases, the behaviour of the transition mass closely resembles that found in the constant accretion case. For the higher-metallicity models ($Z = 0.03$ and $Z = 0.02$), the transition mass remains nearly constant at low average accretion rates and exhibits only a mild increase as the average rate becomes larger.

4.3.1.2 Dependence on α

In Figure (4.3.2) the simulations for models with $\alpha = -1, -2, -3$ are shown assuming a fixed metallicity of $Z = 0.02$. The values are also given in Tables A3.1 and A3.2.

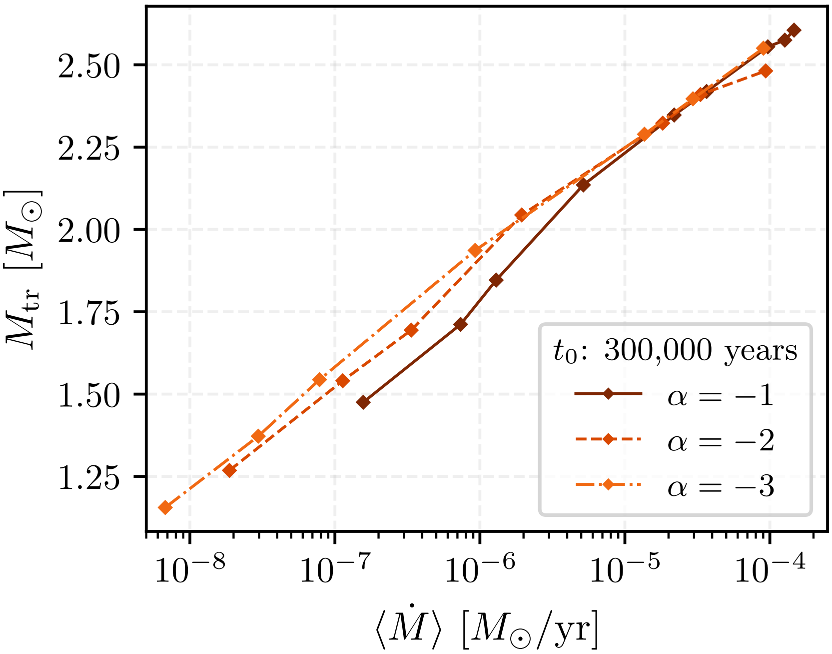

Figure 4.3.2: Results for the models with a power-law accretion rate, as defined in Eq. (4.3.1), assuming $t_0 = 300,000$ years and different power-law indexes, for a solar metallicity. Here, we show the transition mass for which at least 50% of the protostar has become radiative as a function of the average accretion rate defined via Eq.(4.2.2).

For the same initial accretion rates, we can see that the average rate changes by more than an order of magnitude, considering values of α between -1 and -3. Hence, the greatest changes appear to occur at the lower averaged accretion rates, while for the higher ones the curves behave similarly between different values of α, reaching values for the transition mass of $2.61, 2.48$ and 2.55 $\rm M_\odot$ for $\alpha = -1, -2, -3$, respectively.

4.3.2 Comparison of all the models

A comparison between the plots in Figures (4.1.2), (4.2.1), and (4.3.1) is presented in Figure (4.3.3), which includes the results obtained for the different accretion histories we considered and different metallicities. As we can see, metallicity plays a key role in the analysis of the transition between radiative and convective states, while the accretion history appears less relevant.

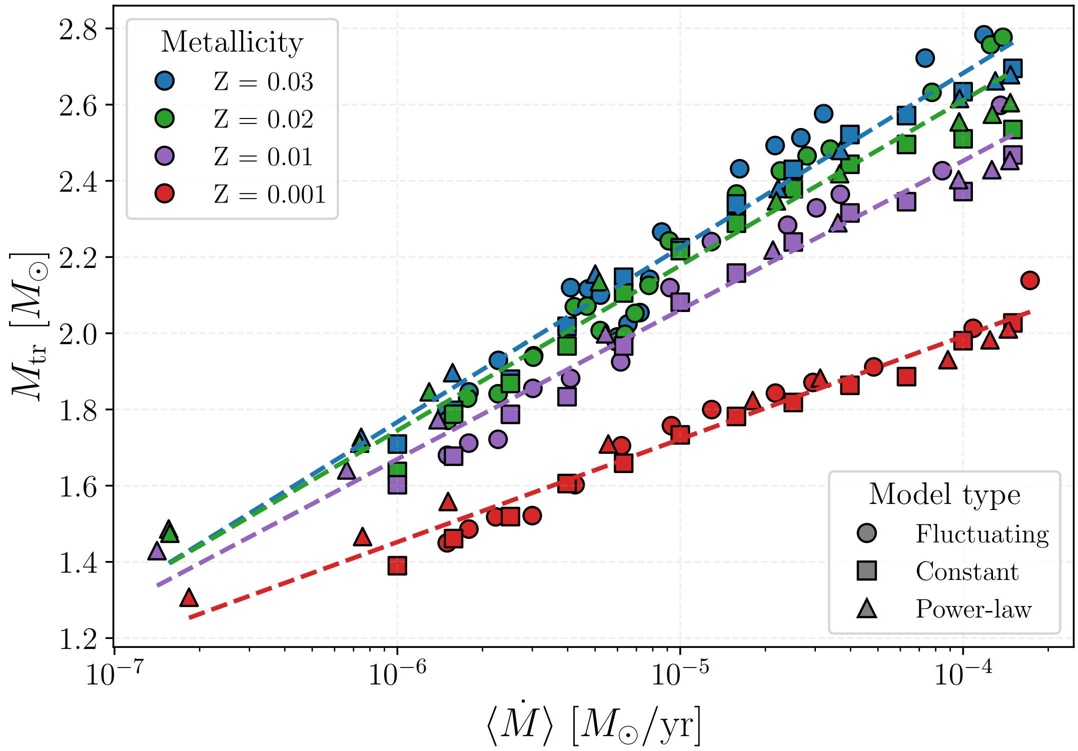

Figure 4.3.3: Overlay of the results from the constant, fluctuating and power-law accretion scenarios, showing the behavior of the transition mass for three different prescriptions of the accretion rate, comparing them with four different metallicities. The lines show the fits to the four different groups and the parameters are given in Table (A2.2).

Chapter 5

Discussion and conclusions

We have presented a series of stellar models using the MESA code to investigate the pre-main-sequence evolution of intermediate-mass stars under different assumptions for the time-evolution of the accretion rate and the protostellar metallicity. In particular, we have considered scenarios with constant, fluctuating, and power-law accretion rates. For metallicity, we have explored a parameter space from 0.001 to 0.03. Our main goal was to determine the transition mass at which the transition occurred from a mostly convective to a mostly radiative state, which we quantified and plotted as a function of the average accretion rate during the protostellar evolution. We generally found that this transition occurs between a minimum mass of ~ 1.3 $M_\odot$ and a maximum mass of ~ 2.8 $M_\odot$. The masses for the transition weakly depend on the average accretion rate and tend to increase with it. A clear dependence on the adopted metallicity has also been found.

We explored to what extent the time evolution of the accretion rate is relevant. As a reference case, we first studied the constant accretion scenario to compare and analyze different accretion rates. As shown in Table (A1.1), the time at which the protostar reaches the transition mass is always shorter for lower metallicities; this is also true for the transition mass itself, which decreases with metallicity. We also note that as the constant accretion rate increases, the values of the transition mass also increase for each metallicity, which are well described by a logarithmic fit (see Table A2.1).

We further looked into the effects of fluctuating accretion rates, considering period variations between 10.000 and 50.000 years, motivated by episodic accretion scenarios. In this case, we found a mostly weak dependence on the adopted accretion period, which only occasionally influenced the point when the transition occurred in cases of somewhat longer periods when the accretion rate had been reduced during the time of the transition. The main dependence also in this case was with respect to the average accretion rate and the metallicity. Also, our last case of a decreasing power-law accretion rate was showing essentially the same behavior, suggesting that at least to first order the time evolution of the accretion is not too relevant, but the average accretion rate and metallicity predominantly govern the point when the transition to a radiative state will occur.

In our models, the transition mass slightly increases with the accretion rate across all prescriptions, but by only about a solar mass, while the average accretion rate has been varied by 2-3 orders of magnitude. This means that the transition to the radiative state will usually occur at a somewhat similar point, between 1 and 2 $M_\odot$. After that transition, magnetic fields can be expected to survive more easily, providing a potential explanation for the larger fraction of stars with magnetic fields at increased stellar masses. Our results suggest that also a dependence on metallicity should be present, implying lower transition masses for lower metallicity, which should translate into larger fractions of stars with strong magnetic fields. Potentially, this prediction can be tested by performing an analysis of the observed samples.

An important caveat concerns the fact that particularly the protostars with higher accretion rates and metallicities of at least $Z = 0.01$ tend to still have a convective outer envelope until reaching the zero-age main sequence. It is possible that in these cases, the accreted magnetic field could be dissipated via convection, even if such a case so far has not been investigated via 3D magneto-hydrodynamical simulations. It is then possible that the observed radiative stars originate predominantly from cases of lower accretion rates, even if it is too early for a definite conclusion. We also emphasize that within this study, we have adopted several simplified toy models for the accretion rate. Preferably, though, it would be desirable to calculate the protostellar evolution considering a sample of time-dependent accretion rate from 3D simulations of intermediate-mass star formation, while so far star formation studies focus predominantly on the low-mass regime (e.g. Riaz et al., 2018, 2021; Wurster et al., 2022) or the high-mass regime (e.g. Peters et al., 2010; Seifried et al., 2013).

We have neglected the effect of rotation in the models presented here, which is difficult to include during a protostellar phase involving accretion, but it can potentially affect the evolution of the internal structure of the protostar and somewhat change the mass scale for the transition. A general limitation is that the MESA code is a 1D model of stellar evolution. Since effects such as rotation and protostellar convection are intrinsically 3D phenomena, and MESA uses simplified recipes based on mixing-length theory, some discrepancies may arise. The presence of the fossil field itself may further alter the convection in the protostars, leading to a slightly different evolution. Similarly, the assumption of cold accretion is a simplification, and more violent accretion events could occasionally also lead to somewhat extended protostellar radii including a possible convective phase. In the long term, it will be important to verify stellar models through detailed 3D simulations. As we are only analyzing the transition to a radiative state for different models, it is also important to note that further exploration of the survival and general interaction between magnetic fields and the internal structure of the star is still required. Although some studies on the survival of these magnetic fields in radiative stars already exist, such as Braithwaite and Spruit (2004), additional systematic investigations are necessary for different stellar environments and magnetic field strengths to fully understand what the origin of these fields is.

Bibliography

A. Eddington, A. S. (1926). *The Internal Constitution of the Stars.*

Alecian, E., Neiner, C., Mathis, S., Catala, C., Kochukhov, O., and Landstreet, J. (2013). The dramatic change of the fossil magnetic field of HD 190073: evidence of the birth of the convective core in a Herbig star? , 549:L8.

Astropy Collaboration, Price-Whelan, A. M., Sipőcz, B. M., Günther, H. M., Lim, P. L., Crawford, S. M., Conseil, S., Shupe, D. L., Craig, M. W., Dencheva, N., Ginsburg, A., VanderPlas, J. T., Bradley, L. D., Pérez-Suárez, D., de Val-Borro, M., Aldcroft, T. L., Cruz, K. L., Robitaille, T. P., Tollerud, E. J., Ardelean, C., Babej, T., Bach, Y. P., Bachetti, M., Bakanov, A. V., Bamford, S. P., Barentsen, G., Barmby, P., Baumbach, A., Berry, K. L., Biscani, F., Boquien, M., Bostroem, K. A., Bouma, L. G., Brammer, G. B., Bray, E. M., Breytenbach, H., Buddelmeijer, H., Burke, D. J., Calderone, G., Cano Rodríguez, J. L., Cara, M., Cardoso, J. V. M., Cheedella, S., Copin, Y., Corrales, L., Crichton, D., D'Avella, D., Deil, C., Depagne, É., Dietrich, J. P., Donath, A., Droettboom, M., Earl, N., Erben, T., Fabbro, S., Ferreira, L. A., Finethy, T., Fox, R. T., Garrison, L. H., Gibbons, S. L. J., Goldstein, D. A., Gommers, R., Greco, J. P., Greenfield, P., Groener, A. M., Grollier, F., Hagen, A., Hirst, P., Homeier, D., Horton, A. J., Hosseinzadeh, G., Hu, L., Hunkeler, J. S., Ivezić, Ž., Jain, A., Jenness, T., Kanarek, G., Kendrew, S., Kern, N. S., Kerzendorf, W. E., Khvalko, A., King, J., Kirkby, D., Kulkarni, A. M., Kumar, A., Lee, A., Lenz, D., Littlefair, S. P., Ma, Z., Macleod, D. M., Mastropietro, M., McCully, C., Montagnac, S., Morris, B. M., Mueller, M., Mumford, S. J., Muna, D., Murphy, N. A., Nelson, S., Nguyen, G. H., Ninan, J. P., Nöthe, M., Ogaz, S., Oh, S., Parejko, J. K., Parley, N., Pascual, S., Patil, R., Patil, A. A., Plunkett, A. L., Prochaska, J. X., Rastogi, T., Reddy Janga, V., Sabater, J., Sakurikar, P., Seifert, M., Sherbert, L. E., Sherwood-Taylor, H., Shih, A. Y., Sick, J., Silbiger, M. T., Singanamalla, S., Singer, L. P., Sladen, P. H., Sooley, K. A., Sornarajah, S., Streicher, O., Teuben, P., Thomas, S. W., Tremblay, G. R., Turner, J. E. H., Terrón, V., van Kerkwijk, M. H., de la Vega, A., Watkins, L. L., Weaver, B. A., Whitmore, J. B., Woillez, J., Zabalza, V., and Astropy Contributors (2018). The Astropy Project: Building an Open-science Project and Status of the v2.0 Core Package. , 156(3):123.

Auddy, S., Basu, S., and Kudoh, T. (2022). The Magnetic Field versus Density Relation in Star-forming Molecular Clouds. , 928(1):L2.

Aurière, M., Wade, G. A., Silvester, J., Lignières, F., Bagnulo, S., Bale, K., Dintrans, B., Donati, J. F., Folsom, C. P., Gruberbauer, M., Hui Bon Hoa, A., Jeffers, S., Johnson, N., Landstreet, J. D., Lèbre, A., Lueftinger, T., Marsden, S., Mouillet, D., Naseri, S., Paletou, F., Petit, P., Power, J., Rincon, F., Strasser, S., and Toqué, N. (2007). Weak magnetic fields in Ap/Bp stars. Evidence for a dipole field lower limit and a tentative interpretation of the magnetic dichotomy. , 475(3):1053–1065.

Baraffe, I., Chabrier, G., Allard, F., and Hauschildt, P. H. (1998). Evolutionary models for solar metallicity low-mass stars: mass-magnitude relationships and color-magnitude diagrams. , 337:403–412.

Becerra, L., Reisenegger, A., Valdivia, J. A., and Gusakov, M. (2022). Stability of axially symmetric magnetic fields in stars. *Monthly Notices of the Royal Astronomical Society*, 517(1):560–568.

Bethe, H. A. (1939). Energy Production in Stars. *Physical Review*, 55(5):434–456.

Biermann, L. (1932). Untersuchungen über den inneren Aufbau der Sterne. IV. Konvektionszonen im Innern der Sterne. (Veröffentlichungen der Universitäts-Sternwarte Göttingen, Nr. 27.) Mit 5 Abbildungen. , 5:117.

Biermann, L. (1938). Konvektion im Innern der Sterne (II). *Astronomische Nachrichten*, 264(22):361.

Biermann, L. (1945). Neuere Fortschritte der Theorie des inneren Aufbaues und der Entwicklung der Sterne. *Ergebnisse der exakten Naturwissenschaften*, 21:1.

Blouin, S., Shaffer, N. R., Saumon, D., and Starrett, C. E. (2020). New Conductive Opacities for White Dwarf Envelopes. , 899(1):46.

Böhm-Vitense, E. (1958). Über die Wasserstoffkonvektionszone in Sternen verschiedener Effektivtemperaturen und Leuchtkräfte. Mit 5 Textabbildungen. , 46:108.

Braithwaite, J. (2008). On non-axisymmetric magnetic equilibria in stars. , 386(4):1947–1958.

Braithwaite, J. and Nordlund, Å. (2006). Stable magnetic fields in stellar interiors. , 450(3):1077–1095.

Braithwaite, J. and Spruit, H. C. (2004). A fossil origin for the magnetic field in A stars and white dwarfs. , 431(7010):819–821.

Braithwaite, J. and Spruit, H. C. (2017). Magnetic fields in non-convective regions of stars. *Royal Society Open Science*, 4(2):160271.

Brandenburg, A. and Subramanian, K. (2005). Astrophysical magnetic fields and nonlinear dynamo theory. , 417(1-4):1–209.

Bressan, A., Marigo, P., Girardi, L., Salasnich, B., Dal Cero, C., Rubele, S., and Nanni, A. (2012). Parsec: stellar tracks and isochrones with the padova and trieste stellar evolution code. *Monthly Notices of the Royal Astronomical Society*, 427(1):127–145.

Brott, I., de Mink, S. E., Cantiello, M., Langer, N., de Koter, A., Evans, C. J., Hunter, I., Trundle, C., and Vink, J. S. (2011). Rotating massive main-sequence stars. I. Grids of evolutionary models and isochrones. , 530:A115.

Browning, M. K., Brun, A. S., and Toomre, J. (2004). Simulations of Core Convection in Rotating A-Type Stars: Differential Rotation and Overshooting. , 601(1):512–529.

Brun, A. S., Browning, M. K., and Toomre, J. (2005). Simulations of core convection in rotating a-type stars: Magnetic dynamo action. *The Astrophysical Journal*, 629(1):461.

Burbidge, E. M., Burbidge, G. R., Fowler, W. A., and Hoyle, F. (1957). Synthesis of the elements in stars. *Rev. Mod. Phys.*, 29:547–650.

Canuto, V. M., Goldman, I., and Mazzitelli, I. (1996). Stellar Turbulent Convection: A Self-consistent Model. , 473:550.

Canuto, V. M. and Mazzitelli, I. (1991). Stellar Turbulent Convection: A New Model and Applications. , 370:295.

Canuto, V. M. and Mazzitelli, I. (1992). Further Improvements of a New Model for Turbulent Convection in Stars. , 389:724.

Chapman, N. L., Davidson, J. A., Goldsmith, P. F., Houde, M., Kwon, W., Li, Z.-Y., Looney, L. W., Matthews, B., Matthews, T. G., Novak, G., Peng, R., Vaillancourt, J. E., and Volgenau, N. H. (2013). Alignment between Flattened Protostellar Infall Envelopes and Ambient Magnetic Fields. , 770(2):151.

Choi, J., Dotter, A., Conroy, C., Cantiello, M., Paxton, B., and Johnson, B. D. (2016). Mesa Isochrones and Stellar Tracks (MIST). I. Solar-scaled Models. , 823(2):102.

Choudhuri, A. R. (1998). *The Physics of Fluids and Plasmas: An Introduction for Astrophysicists.*

Cowling, T. G. (1945). On the Sun's general magnetic field. , 105:166.

Cox, J. P. and Giuli, R. T. (1968). *Principles of stellar structure.*

Crutcher, R. M. (2012). Magnetic Fields in Molecular Clouds. , 50:29–63.

Desch, S. J. and Mouschovias, T. C. (2001). The magnetic decoupling stage of star formation. *The Astrophysical Journal*, 550(1):314.

Donati, J. F. and Landstreet, J. D. (2009). Magnetic Fields of Nondegenerate Stars. , 47(1):333–370.

Dudorov, A. E. and Khaibrakhmanov, S. A. (2015). Theory of fossil magnetic field. *Advances in Space Research*, 55(3):843–850.

Dudorov, A. E. and Tutukov, A. V. (1990). The Magnetic Field of CP Stars. , 34:171.

Eggleton, P. P. (1971). The evolution of low mass stars. , 151:351.

Ekström, S., Georgy, C., Eggenberger, P., Meynet, G., Mowlavi, N., Wyttenbach, A., Granada, A., Decressin, T., Hirschi, R., Frischknecht, U., Charbonnel, C., and Maeder, A. (2012). Grids of stellar models with rotation - i. models from 0.8 to 120 m at solar metallicity (z = 0.014). *AA*, 537:A146.

Emden, R. (1902). Contributions to the Solar Theory. , 15:38.

Emden, R. (1907). *Gaskugeln*.

Featherstone, N. A., Browning, M. K., Brun, A. S., and Toomre, J. (2009). Effects of Fossil Magnetic Fields on Convective Core Dynamos in A-type Stars. , 705(1):1000–1018.

Ferguson, J. W., Alexander, D. R., Allard, F., Barman, T., Bodnarik, J. G., Hauschildt, P. H., Heffner-Wong, A., and Tamanai, A. (2005). Low-Temperature Opacities. , 623(1):585–596.

Foreman-Mackey, D., Hogg, D. W., Lang, D., and Goodman, J. (2013). emcee: The MCMC Hammer. , 125(925):306.

Gautschy, A. (2018). The theorem that was none - II. The profound 70s. *arXiv e-prints*, page arXiv:1812.11864.

Georgy, C., Ekström, S., Eggenberger, P., Meynet, G., Haemmerlé, L., Maeder, A., Granada, A., Groh, J. H., Hirschi, R., Mowlavi, N., Yusof, N., Charbonnel, C., Decressin, T., and Barblan, F. (2013). Grids of stellar models with rotation. III. Models from 0.8 to 120 $M_\odot$ at a metallicity Z = 0.002. , 558:A103.

Girardi, L., Bertelli, G., Bressan, A., Chiosi, C., Groenewegen, M. A. T., Marigo, P., Salasnich, B., and Weiss, A. (2002). Theoretical isochrones in several photometric systems. I. Johnson-Cousins-Glass, HST/WFPC2, HST/NICMOS, Washington, and ESO Imaging Survey filter sets. , 391:195–212.

Girart, J. M., Rao, R., and Marrone, D. P. (2006). Magnetic Fields in the Formation of Sun-Like Stars. *Science*, 313(5788):812–814.

Gough, D. O. (1977). Mixing-length theory for pulsating stars. , 214:196–213.

Gough, D. O. and Weiss, N. O. (1976). The calibration of stellar convection theories. *Monthly Notices of the Royal Astronomical Society*, 176(3):589–607.

Grevesse, N. and Sauval, A. J. (1998). Standard Solar Composition. , 85:161–174.

Guenther, E. W., Lehmann, H., Emerson, J. P., and Staude, J. (1999). Measurements of magnetic field strength on T Tauri stars. , 341:768–783.

Haemmerlé, L., Eggenberger, P., Meynet, G., Maeder, A., and Charbonnel, C.

(2013). Star formation with disc accretion and rotation. I. Stars between 2 and 22 $M_\odot$ at solar metallicity. , 557:A112.

Henyey, L., Vardya, M. S., and Bodenheimer, P. (1965). Studies in Stellar Evolution. III. The Calculation of Model Envelopes. , 142:841.

Henyey, L. G., Forbes, J. E., and Gould, N. L. (1964). A New Method of Automatic Computation of Stellar Evolution. , 139:306.

Hertzsprung, E. (1911). Ueber die Verwendung photographischer effektiver Wellenlaengen zur Bestimmung von Farbenaequivalenten. *Publikationen des Astrophysikalischen Observatoriums zu Potsdam*, 63.

Hidalgo, J. P., Käpylä, P. J., Schleicher, D. R. G., Ortiz-Rodríguez, C. A., and Navarrete, F. H. (2024). Magnetohydrodynamic simulations of A-type stars: Long-term evolution of core dynamo cycles. , 691:A326.

Hidalgo, J. P., Käpylä, P. J., Schleicher, D. R. G., Ortiz-Rodríguez, C. A., and Navarrete, F. H. (2025). Shaping core dynamos in A-type stars: The role of dipolar fossil fields. , 699:A250.

Hosokawa, T., Yorke, H. W., and Omukai, K. (2010). Evolution of Massive Protostars Via Disk Accretion. , 721(1):478–492.

Jermyn, A. S., Bauer, E. B., Schwab, J., Farmer, R., Ball, W. H., Bellinger, E. P., Dotter, A., Joyce, M., Marchant, P., Mombarg, J. S. G., Wolf, W. M., Sunny Wong, T. L., Cinquegrana, G. C., Farrell, E., Smolec, R., Thoul, A., Cantiello, M., Herwig, F., Toloza, O., Bildsten, L., Townsend, R. H. D., and Timmes, F. X. (2023). Modules for Experiments in Stellar Astrophysics (MESA): Time-dependent Convection, Energy Conservation, Automatic Differentiation, and Infrastructure. , 265(1):15.

Johns-Krull, C. M. (2007). The Magnetic Fields of Classical T Tauri Stars. , 664(2):975–985.

Käpylä, P. J., Browning, M. K., Brun, A. S., Guerrero, G., and Warnecke, J. (2023). Simulations of Solar and Stellar Dynamos and Their Theoretical Interpretation. , 219(7):58.

Kippenhahn, R., Weigert, A., and Weiss, A. (2012). *Stellar Structure and Evolution.*

Kochukhov, O. (2021). Magnetic fields of M dwarfs. , 29(1):1.

Koley, A., Roy, N., Momjian, E., Sarma, A. P., and Datta, A. (2022). Magnetic field measurement in TMC-1C using 22.3 GHz CCS Zeeman splitting. , 516(1):L48–L52.

Laplace, E. (2022). TULIPS: A Tool for Understanding the Lives, Interiors, and Physics of Stars. *Astronomy and Computing*, 38:100516.

Larson, R. B. (1969). Numerical calculations of the dynamics of collapsing proto-star. , 145:271.

Lavail, A., Kochukhov, O., Hussain, G. A. J., Alecian, E., Herczeg, G. J., and Johns-Krull, C. (2017). Magnetic fields of intermediate mass T Tauri stars. , 608:A77.

Lecoanet, D., Bowman, D. M., and Van Reeth, T. (2022). Asteroseismic inference of the near-core magnetic field strength in the main-sequence B star HD 43317. , 512(1):L16–L20.

Li, H.-b., Dowell, C. D., Goodman, A., Hildebrand, R., and Novak, G. (2009). Anchoring Magnetic Field in Turbulent Molecular Clouds. , 704(2):891–897.

MacDonald, J. and Mullan, D. J. (2004). Magnetic fields in massive stars: dynamics and origin. *Monthly Notices of the Royal Astronomical Society*, 348(2):702–716.

MacGregor, K. B. and Cassinelli, J. P. (2003). Magnetic fields in massive stars. ii. the buoyant rise of magnetic flux tubes through the radiative interior. *The Astrophysical Journal*, 586(1):480.

Masson, J., Chabrier, G., Hennebelle, P., Vaytet, N., and Commerçon, B. (2016). Ambipolar diffusion in low-mass star formation. I. General comparison with the ideal magnetohydrodynamic case. , 587:A32.

Mathys, G. (2008). Extremely slowly rotating magnetic Ap stars: recent results. *Contributions of the Astronomical Observatory Skalnate Pleso*, 38(2):217–222.

Mathys, G. (2017). Ap stars with resolved magnetically split lines: Magnetic field determinations from Stokes I and V spectra$\star$. , 601:A14.

Moss, D. (1989). The origin and internal structure of the magnetic fields of the CP stars. , 236:629–644.

Nakano, T. (1988). The Behaviour of Magnetic Fields in Star Forming Regions. In Pudritz, R. E. and Fich, M., editors, *Galactic and Extragalactic Star Formation*, volume 232 of *NATO Advanced Study Institute (ASI) Series C*, page 111.

Nakano, T., Nishi, R., and Umebayashi, T. (2002). Mechanism of Magnetic Flux Loss in Molecular Clouds. , 573(1):199–214.

Nakano, T. and Umebayashi, T. (1988). Chapter 6. effects of magnetic fields on star formation. *Progress of Theoretical Physics Supplement*, 96:73–84.

Ness, M., Hogg, D. W., Rix, H.-W., Ho, A. Y. Q., and Zasowski, G. (2015). The Cannon: A data-driven approach to Stellar Label Determination. , 808(1):16.

Paczyński, B. (1970). Evolution of Single Stars. I. Stellar Evolution from Main Sequence to White Dwarf or Carbon Ignition. , 20:47.

Palla, F. and Stahler, S. W. (1990). The Birthline for Intermediate-Mass Stars. , 360:L47.

Palla, F. and Stahler, S. W. (1991). The Evolution of Intermediate-Mass Protostars. I. Basic Results. , 375:288.

Palla, F. and Stahler, S. W. (1992). The Evolution of Intermediate-Mass Protostars. II. Influence of the Accretion Flow. , 392:667.

Palla, F. and Stahler, S. W. (2000). Accelerating Star Formation in Clusters and Associations. , 540(1):255–270.

Paxton, B., Bildsten, L., Dotter, A., Herwig, F., Lesaffre, P., and Timmes, F. (2011). Modules for Experiments in Stellar Astrophysics (MESA). , 192(1):3.

Paxton, B., Cantiello, M., Arras, P., Bildsten, L., Brown, E. F., Dotter, A., Mankovich, C., Montgomery, M. H., Stello, D., Timmes, F. X., and Townsend, R. (2013). Modules for Experiments in Stellar Astrophysics (MESA): Planets, Oscillations, Rotation, and Massive Stars. , 208(1):4.

Paxton, B., Marchant, P., Schwab, J., Bauer, E. B., Bildsten, L., Cantiello, M., Dessart, L., Farmer, R., Hu, H., Langer, N., Townsend, R. H. D., Townsley, D. M., and Timmes, F. X. (2015). Modules for Experiments in Stellar Astrophysics (MESA): Binaries, Pulsations, and Explosions. , 220(1):15.

Paxton, B., Smolec, R., Schwab, J., Gautschy, A., Bildsten, L., Cantiello, M., Dotter, A., Farmer, R., Goldberg, J. A., Jermyn, A. S., Kanbur, S. M., Marchant, P., Thoul, A., Townsend, R. H. D., Wolf, W. M., Zhang, M., and Timmes, F. X. (2019). Modules for Experiments in Stellar Astrophysics (MESA): Pulsating Variable Stars, Rotation, Convective Boundaries, and Energy Conservation. , 243(1):10.

Peters, T., Klessen, R. S., Mac Low, M.-M., and Banerjee, R. (2010). Limiting Accretion onto Massive Stars by Fragmentation-induced Starvation. , 725(1):134–145.

Pols, O. R., Tout, C. A., Eggleton, P. P., and Han, Z. (1995). Approximate input physics for stellar modelling. *Monthly Notices of the Royal Astronomical Society*, 274(3):964–974.

Power, J., Wade, G. A., Hanes, D. A., Aurier, M., and Silvester, J. (2007). Properties of a volume-limited sample of magnetic Ap/Bp stars. In Romanyuk, I. I., Kudryavtsev, D. O., Neizvestnaya, O. M., and Shapoval, V. M., editors, *Physics of Magnetic Stars*, pages 89–97.

Prandtl, L. (1925). 7. Bericht über Untersuchungen zur ausgebildeten Turbulenz. *Zeitschrift Angewandte Mathematik und Mechanik*, 5(2):136–139.

Riaz, R., Schleicher, D. R. G., Vanaverbeke, S., and Klessen, R. S. (2021). Turbulence and its connection to episodic accretion in binary YSOs. , 507(4):6061–6077.

Riaz, R., Vanaverbeke, S., and Schleicher, D. R. G. (2018). Episodic accretion in binary protostars emerging from self-gravitating solar mass cores. , 614:A53.

Rogers, F. J. and Nayfonov, A. (2002). Updated and Expanded OPAL Equation-of-State Tables: Implications for Helioseismology. , 576(2):1064–1074.

Russell, H. N. (1914). Relations Between the Spectra and Other Characteristics of the Stars. *Popular Astronomy*, 22:331–351.

Saumon, D., Chabrier, G., and van Horn, H. M. (1995). An Equation of State for Low-Mass Stars and Giant Planets. , 99:713.

Schleicher, D. R. G., Hidalgo, J. P., and Galli, D. (2023). Survival of fossil fields during the pre-main sequence evolution of intermediate-mass stars. , 678:A204.

Schmidt, A. (1917). Deutsche Meteorologische Gesellschaft: Berliner Zweigverein. *Naturwissenschaften*, 5(47):710–711.

Schwarzschild, M. (1958). *Structure and evolution of the stars.*

Seifried, D., Banerjee, R., Pudritz, R. E., and Klessen, R. S. (2013). Turbulence-induced disc formation in strongly magnetized cloud cores. , 432(4):3320–3331.

Taylor, G. I. (1915). Eddy Motion in the Atmosphere. *Philosophical Transactions of the Royal Society of London Series A*, 215:1–26.

Tomida, K., Okuzumi, S., and Machida, M. N. (2015). Radiation Magnetohydrodynamic Simulations of Protostellar Collapse: Nonideal Magnetohydrodynamic Effects and Early Formation of Circumstellar Disks. , 801(2):117.

Turk, M. J., Smith, B. D., Oishi, J. S., Skory, S., Skillman, S. W., Abel, T., and Norman, M. L. (2011). yt: A Multi-code Analysis Toolkit for Astrophysical Simulation Data. , 192(1):9.

Vallee, J. P. (1997). Observations of the Magnetic Fields Inside and Outside the Milky Way, Starting with Globules (~1 parsec), Filaments, Clouds, Superbubbles, Spiral Arms, Galaxies, Superclusters, and Ending with the Cosmological Universe's Background Surface (at ~8 Teraparsecs). , 19:1–89.

Vidotto, A. A., Gregory, S. G., Jardine, M., Donati, J. F., Petit, P., Morin, J., Folsom, C. P., Bouvier, J., Cameron, A. C., Hussain, G., Marsden, S., Waite, I. A., Fares, R., Jeffers, S., and do Nascimento, J. D. (2014). Stellar magnetism: empirical trends with age and rotation. , 441(3):2361–2374.

Wurster, J., Bate, M. R., Price, D. J., and Bonnell, I. A. (2022). On the origin of magnetic fields in stars - II. The effect of numerical resolution. , 511(1):746–764.

Xiong (1978). Stochastic theory of turbulent convection in pulsating variables. *Chinese Astronomy*, 2(1):118–138.

Xiong (1980). A statistical theory of non-local convection. *Chinese Astronomy*, 4(3):234–242.

Xiong (2021). Convection theory and relevant problems in stellar structure, evolution, and pulsational stability i convection theory and structure of convection zone and stellar evolution. *Frontiers in Astronomy and Space Sciences*, Volume 7 - 2020.

Appendix A

Data and plots from the one-dimensional simulations

A1 Data for constant mass accretion rate scenario

In Table A1.1, we provide the main results in case of the constant accretion rate scenario described in Section for four different metallicities.

Table A1.1: Results from the constant mass accretion rate scenario described in Section (4.1). Here are shown the constant accretion rate $\dot{M}$, the mass and time of the transition M_{tr} and t_{tr}, and the mass at the zero-age main sequence M_{ZAMS} for four distinct metallicities.

$\dot{M}$	$Z = 0.001$			$Z = 0.01$		
$[\mathrm{M}_{\odot}\mathrm{yr}^{-1}]$	M_{tr} $[\mathrm{M}_{\odot}]$	t_{tr} [Myr]	M_{ZAMS} $[\mathrm{M}_{\odot}]$	M_{tr} $[\mathrm{M}_{\odot}]$	t_{tr} [Myr]	M_{ZAMS} $[\mathrm{M}_{\odot}]$
$1.00 \cdot 10^{-6}$	1.39	0.39	2.93	1.60	0.60	3.21
$1.58 \cdot 10^{-6}$	1.46	0.29	3.27	1.68	0.43	3.55
$2.51 \cdot 10^{-6}$	1.52	0.21	3.67	1.79	0.31	3.92
$3.98 \cdot 10^{-6}$	1.61	0.15	4.11	1.83	0.21	4.31
$6.31 \cdot 10^{-6}$	1.66	0.10	4.60	1.97	0.15	4.76
$1.00 \cdot 10^{-5}$	1.73	0.07	5.15	2.08	0.11	5.20
$1.58 \cdot 10^{-5}$	1.78	0.05	5.75	2.16	0.07	3.62
$2.51 \cdot 10^{-5}$	1.82	0.03	6.42	2.24	0.05	3.37
$3.98 \cdot 10^{-5}$	1.86	0.02	7.13	2.32	0.03	3.29
$6.31 \cdot 10^{-5}$	1.89	0.01	7.88	2.35	0.02	3.24
$1.00 \cdot 10^{-4}$	1.98	0.01	4.50	2.37	0.01	3.21
$1.50 \cdot 10^{-4}$	2.03	0.01	4.31	2.47	0.01	3.19

$\dot{\mathrm{M}}$	$Z = 0.02$			$Z = 0.03$		
$[\mathrm{M}_{\odot}\,\mathrm{yr}^{-1}]$	M_{tr} $[\mathrm{M}_{\odot}]$	t_{tr} [Myr]	M_{ZAMS} $[\mathrm{M}_{\odot}]$	M_{tr} $[\mathrm{M}_{\odot}]$	t_{tr} [Myr]	M_{ZAMS} $[\mathrm{M}_{\odot}]$
$1.00 \cdot 10^{-6}$	1.64	0.64	3.43	1.71	0.71	2.96
$1.58 \cdot 10^{-6}$	1.79	0.50	3.78	1.80	0.50	3.96
$2.51 \cdot 10^{-6}$	1.87	0.35	4.19	1.88	0.35	4.39
$3.98 \cdot 10^{-6}$	1.97	0.24	4.63	2.02	0.26	4.87
$6.31 \cdot 10^{-6}$	2.11	0.18	5.11	2.15	0.18	3.09
$1.00 \cdot 10^{-5}$	2.22	0.12	3.19	2.22	0.12	2.93
$1.58 \cdot 10^{-5}$	2.29	0.08	3.06	2.34	0.08	2.86
$2.51 \cdot 10^{-5}$	2.38	0.05	2.99	2.43	0.06	2.82
$3.98 \cdot 10^{-5}$	2.44	0.04	2.96	2.52	0.04	2.79
$6.31 \cdot 10^{-5}$	2.50	0.02	2.93	2.57	0.02	2.77
$1.00 \cdot 10^{-4}$	2.51	0.02	2.91	2.63	0.02	2.76
$1.50 \cdot 10^{-4}$	2.53	0.01	2.90	2.70	0.01	2.75

A2 Fit to the data

In order to model the relation between the transition mass and the mean mass accretion rate, we performed a logarithmic fit to the data in the following form.

$$M_{\rm tr} = a \log_{10}\left(\langle \dot{M} \rangle\right) + b \tag{A2.1}$$

where a and b are free parameters obtained from the fit. The values of the parameters obtained for the constant accretion scenario are summarized in Table A2.1 and the fit results for the entire dataset, including the different models, are in Table A2.2.

Table A2.1: Fit for constant mass accretion rates scenario using Eq. (A2.1). Here we show the metallicity Z and the parameters a, b that best fit the data.

Z	a	b	Equation
0.03	0.4689	4.5462	$M_{\rm tr} = 0.4689 \log_{10}(\dot{M}) + 4.5462$
0.02	0.4226	4.2578	$M_{\rm tr} = 0.4226 \log_{10}(\dot{M}) + 4.2578$
0.01	0.4037	4.0497	$M_{\rm tr} = 0.4037 \log_{10}(\dot{M}) + 4.0497$
0.001	0.2822	3.1105	$M_{\rm tr} = 0.2822 \log_{10}(\dot{M}) + 3.1105$

Table A2.2: Fitting parameters from Eq. (A2.1) applied to the three different prescriptions shown in Figure (4.3.3) grouped by their metallicities. Here are shown the metallicity Z and the parameters a, b that best fit the data.

Z	a	b	Equation
0.03	0.4578	4.5138	$M_{\rm tr} = 0.4578 \log_{10}(\dot{M}) + 4.5138$
0.02	0.4331	4.3435	$M_{\rm tr} = 0.4331 \log_{10}(\dot{M}) + 4.3435$
0.01	0.3913	4.0178	$M_{\rm tr} = 0.3913 \log_{10}(\dot{M}) + 4.0178$
0.001	0.2701	3.0727	$M_{\rm tr} = 0.2701 \log_{10}(\dot{M}) + 3.0727$

A3 Data for the power-law mass accretion rate scenario

In this appendix, we provide the main results for the power-law accretion rate scenario for different metallicities and considering variations of the power-law index.

A3.1 Simulations for power-law index variation

In Table A3.1 and A3.2, we summarize the results for the case of a solar metallicity varying the power-law index α. The table for $\alpha = -1$ was omitted because the data is already in Table A3.5.

Table A3.1: Results for the power-law mass accretion rate scenario, described in Section (4.3.1). We assume a metallicity $Z = 0.02$ and $t_0 =$ 300,000 years.

$\alpha = -3$					
$\dot{M}_0$ [$\mathrm{M}_\odot\,\mathrm{yr}^{-1}$]	M_{ZAMS} [$\mathrm{M}_\odot$]	t_{ZAMS} [Myr]	$\langle\dot{M}\rangle$ [$\mathrm{M}_\odot\,\mathrm{yr}^{-1}$]	M_{tr} [$\mathrm{M}_\odot$]	t_{tr} [Myr]
$1.00 \cdot 10^{-6}$	1.16	23.19	$6.76 \cdot 10^{-9}$	1.16	3.35
$2.51 \cdot 10^{-6}$	1.39	13.07	$2.96 \cdot 10^{-8}$	1.37	1.29
$3.98 \cdot 10^{-6}$	1.61	7.79	$7.83 \cdot 10^{-8}$	1.54	0.64
$1.00 \cdot 10^{-5}$	2.48	1.59	$9.27 \cdot 10^{-7}$	1.94	0.19
$2.51 \cdot 10^{-5}$	3.15	0.16	$1.37 \cdot 10^{-5}$	2.29	0.07
$3.98 \cdot 10^{-5}$	2.99	0.07	$2.95 \cdot 10^{-5}$	2.40	0.04
$1.00 \cdot 10^{-4}$	2.92	0.02	$9.03 \cdot 10^{-5}$	2.55	0.02

Table A3.2: Same as Table A3.1, but with $\alpha = -2$.

$\alpha = -2$					
$\dot{M}_0$ [$\mathrm{M}_\odot\,\mathrm{yr}^{-1}$]	M_{ZAMS} [$\mathrm{M}_\odot$]	t_{ZAMS} [Myr]	$\langle\dot{M}\rangle$ [$\mathrm{M}_\odot\,\mathrm{yr}^{-1}$]	M_{tr} [$\mathrm{M}_\odot$]	t_{tr} [Myr]
$1.00 \cdot 10^{-6}$	1.30	16.16	$1.87 \cdot 10^{-8}$	1.27	2.05
$2.51 \cdot 10^{-6}$	1.73	6.45	$1.13 \cdot 10^{-7}$	1.54	0.73
$3.98 \cdot 10^{-6}$	2.11	3.29	$3.36 \cdot 10^{-7}$	1.69	0.41
$1.00 \cdot 10^{-5}$	3.43	1.25	$1.94 \cdot 10^{-6}$	2.04	0.16
$2.51 \cdot 10^{-5}$	3.06	0.11	$1.82 \cdot 10^{-5}$	2.32	0.06
$3.98 \cdot 10^{-5}$	2.98	0.06	$3.32 \cdot 10^{-5}$	2.41	0.04
$1.00 \cdot 10^{-4}$	2.92	0.02	$9.36 \cdot 10^{-5}$	2.48	0.02

A3.2 Simulations for metallicity variations

In Tables A3.3–A3.6, we summarize the results for the case of a power-law index $\alpha = -1$ varying the metallicity.

Table A3.3: Results from the power-law mass accretion rate scenario described in Section (4.3.1). We assumed a power-law index of $\alpha = -1$ and a $t_0 = 300,000$ years. Here are shown the initial accretion rate $\dot{M}_0$, the mass M_{ZAMS} and time t_{ZAMS} when the star reaches the ZAMS phase, the mean accretion rate of its evolution $\langle \dot{M} \rangle$ calculated according to Eqn. (4.2.2), the mass and time of the transition $M_{\rm tr}$ and $t_{\rm tr}$, respectively for four different metallicities.

$Z = 0.001$					
$\dot{M}_0$ $[M_\odot\,{\rm yr}^{-1}]$	$M_{\rm ZAMS}$ $[M_\odot]$	$t_{\rm ZAMS}$ [Myr]	$\langle \dot{M} \rangle$ $[M_\odot\,{\rm yr}^{-1}]$	$M_{\rm tr}$ $[M_\odot]$	$t_{\rm tr}$ [Myr]
$1.00 \cdot 10^{-6}$	1.84	4.59	$1.83 \cdot 10^{-7}$	1.31	0.53
$2.51 \cdot 10^{-6}$	2.56	2.07	$7.53 \cdot 10^{-7}$	1.47	0.26
$3.98 \cdot 10^{-6}$	3.04	1.35	$1.51 \cdot 10^{-6}$	1.56	0.18
$1.00 \cdot 10^{-5}$	4.24	0.58	$5.57 \cdot 10^{-6}$	1.71	0.08
$2.51 \cdot 10^{-5}$	5.73	0.26	$1.81 \cdot 10^{-5}$	1.82	0.03
$3.98 \cdot 10^{-5}$	6.56	0.18	$3.13 \cdot 10^{-5}$	1.88	0.02
$1.00 \cdot 10^{-4}$	8.30	0.08	$8.83 \cdot 10^{-5}$	1.93	0.01
$1.30 \cdot 10^{-4}$	4.38	0.03	$1.25 \cdot 10^{-4}$	1.98	0.01
$1.50 \cdot 10^{-4}$	4.32	0.02	$1.45 \cdot 10^{-4}$	2.01	0.01

Table A3.4: Same as Table A3.3, but for metallicity $Z = 0.01$.

$Z = 0.01$					
$\dot{M}_0$ $[M_\odot\,{\rm yr}^{-1}]$	$M_{\rm ZAMS}$ $[M_\odot]$	$t_{\rm ZAMS}$ [Myr]	$\langle \dot{M} \rangle$ $[M_\odot\,{\rm yr}^{-1}]$	$M_{\rm tr}$ $[M_\odot]$	$t_{\rm tr}$ [Myr]
$1.00 \cdot 10^{-6}$	1.95	6.74	$1.41 \cdot 10^{-7}$	1.43	0.94
$2.51 \cdot 10^{-6}$	2.71	2.58	$6.62 \cdot 10^{-7}$	1.64	0.40
$3.98 \cdot 10^{-6}$	3.19	1.58	$1.39 \cdot 10^{-6}$	1.77	0.27
$1.00 \cdot 10^{-5}$	4.35	0.62	$5.44 \cdot 10^{-6}$	2.00	0.12
$2.51 \cdot 10^{-5}$	3.43	0.11	$2.13 \cdot 10^{-5}$	2.22	0.05
$3.98 \cdot 10^{-5}$	3.30	0.06	$3.61 \cdot 10^{-5}$	2.29	0.03
$1.00 \cdot 10^{-4}$	3.21	0.02	$9.64 \cdot 10^{-5}$	2.40	0.01
$1.30 \cdot 10^{-4}$	3.19	0.02	$1.26 \cdot 10^{-4}$	2.43	0.01
$1.50 \cdot 10^{-4}$	3.19	0.02	$1.46 \cdot 10^{-4}$	2.45	0.01

Table A3.5: Same as Table A3.3, but for metallicity $Z = 0.02$.

$Z = 0.02$					
$\dot{M}_0$ $[M_\odot\,\mathrm{yr}^{-1}]$	M_{ZAMS} $[M_\odot]$	t_{ZAMS} [Myr]	$\langle\dot{M}\rangle$ $[M_\odot\,\mathrm{yr}^{-1}]$	M_{tr} $[M_\odot]$	t_{tr} [Myr]
$1.00 \cdot 10^{-6}$	1.91	5.80	$1.57 \cdot 10^{-7}$	1.48	1.15
$2.51 \cdot 10^{-6}$	2.59	2.16	$7.36 \cdot 10^{-7}$	1.71	0.47
$3.98 \cdot 10^{-6}$	3.33	1.80	$1.30 \cdot 10^{-6}$	1.85	0.31
$1.00 \cdot 10^{-5}$	4.61	0.70	$5.17 \cdot 10^{-6}$	2.14	0.14
$2.51 \cdot 10^{-5}$	3.02	0.09	$2.19 \cdot 10^{-5}$	2.35	0.06
$3.98 \cdot 10^{-5}$	2.97	0.05	$3.66 \cdot 10^{-5}$	2.42	0.04
$1.00 \cdot 10^{-4}$	2.92	0.02	$9.68 \cdot 10^{-5}$	2.55	0.02
$1.30 \cdot 10^{-4}$	2.91	0.01	$1.27 \cdot 10^{-4}$	2.57	0.01
$1.50 \cdot 10^{-4}$	2.91	0.01	$1.47 \cdot 10^{-4}$	2.61	0.01

Table A3.6: Same as Table A3.3, but for metallicity $Z = 0.03$.

$Z = 0.03$					
$\dot{M}_0$ $[M_\odot\,\mathrm{yr}^{-1}]$	M_{ZAMS} $[M_\odot]$	t_{ZAMS} [Myr]	$\langle\dot{M}\rangle$ $[M_\odot\,\mathrm{yr}^{-1}]$	M_{tr} $[M_\odot]$	t_{tr} [Myr]
$1.00 \cdot 10^{-6}$	1.91	5.88	$1.56 \cdot 10^{-7}$	1.49	1.20
$2.51 \cdot 10^{-6}$	2.58	2.12	$7.45 \cdot 10^{-7}$	1.73	0.49
$3.98 \cdot 10^{-6}$	2.97	1.26	$1.57 \cdot 10^{-6}$	1.90	0.33
$1.00 \cdot 10^{-5}$	4.78	0.75	$5.01 \cdot 10^{-6}$	2.16	0.14
$2.51 \cdot 10^{-5}$	2.83	0.08	$2.22 \cdot 10^{-5}$	2.38	0.06
$3.98 \cdot 10^{-5}$	2.79	0.05	$3.69 \cdot 10^{-5}$	2.48	0.04
$1.00 \cdot 10^{-4}$	2.75	0.02	$9.71 \cdot 10^{-5}$	2.62	0.02
$1.30 \cdot 10^{-4}$	2.75	0.01	$1.30 \cdot 10^{-4}$	2.66	0.01
$1.50 \cdot 10^{-4}$	2.75	0.01	$1.47 \cdot 10^{-4}$	2.68	0.01

A4 Data for the fluctuating mass accretion rate scenario

A4.1 Simulations for variations of the period

In Table A4.1 and A4.2, we summarize the results for the case of a solar metallicity varying the period of the assumed fluctuations.

Table A4.1: Results for the fluctuating mass accretion rate scenario described in Section (4.2.0.1). Here are shown the mass M_{ZAMS} and time t_{ZAMS} when the star reaches the ZAMS phase, the mean accretion rate of its evolution $\langle \dot{M} \rangle$ calculated according to Eqn. (4.2.2), the transition mass $M_{\rm tr}$ and the transition time $t_{\rm tr}$ for different values of the period P and the amplitude A. For these calculation, we assumed a metallicity of $Z = 0.02$.

$P = 10{,}000$					
Amplitude $[M_\odot\,{\rm yr}^{-1}]$	$M_{\rm ZAMS}$ $[M_\odot]$	$t_{\rm ZAMS}$ [Myr]	$\langle \dot{M} \rangle \cdot 10^{-6}$ $[M_\odot\,{\rm yr}^{-1}]$	$M_{\rm tr}$ $[M_\odot]$	$t_{\rm tr}$ [Myr]
$1.00 \cdot 10^{-6}$	3.75	1.85	1.49	1.75	0.51
$1.58 \cdot 10^{-6}$	3.32	1.32	1.75	1.81	0.46
$2.51 \cdot 10^{-6}$	3.41	1.10	2.19	1.84	0.39
$3.98 \cdot 10^{-6}$	3.61	0.91	2.87	1.90	0.32
$6.31 \cdot 10^{-6}$	3.85	0.72	3.96	1.98	0.25
$1.00 \cdot 10^{-5}$	4.04	0.53	5.71	2.07	0.19
$1.58 \cdot 10^{-5}$	4.19	0.38	8.43	2.15	0.14
$2.51 \cdot 10^{-5}$	3.12	0.17	12.47	2.24	0.09
$3.98 \cdot 10^{-5}$	3.04	0.11	19.08	2.30	0.06
$6.31 \cdot 10^{-5}$	2.97	0.06	33.83	2.48	0.05
$1.00 \cdot 10^{-4}$	2.96	0.04	44.97	2.49	0.02
$3.98 \cdot 10^{-4}$	2.94	0.01	153.5	2.74	0.01

Table A4.2: Same as Table A4.1, but for a period $P = 25{,}000$ years.

$P = 25{,}000$					
Amplitude $[M_\odot\,{\rm yr}^{-1}]$	$M_{\rm ZAMS}$ $[M_\odot]$	$t_{\rm ZAMS}$ [Myr]	$\langle \dot{M} \rangle \cdot 10^{-6}$ $[M_\odot\,{\rm yr}^{-1}]$	$M_{\rm tr}$ $[M_\odot]$	$t_{\rm tr}$ [Myr]
$1.00 \cdot 10^{-6}$	3.23	1.49	1.50	1.76	0.51
$1.58 \cdot 10^{-6}$	3.37	1.33	1.78	1.81	0.45
$2.51 \cdot 10^{-6}$	3.45	1.09	2.25	1.85	0.37
$3.98 \cdot 10^{-6}$	3.55	0.87	2.95	1.92	0.30
$6.31 \cdot 10^{-6}$	3.89	0.69	4.16	1.98	0.24
$1.00 \cdot 10^{-5}$	4.23	0.54	6.02	2.03	0.18
$1.58 \cdot 10^{-5}$	3.33	0.27	8.62	2.26	0.13
$2.51 \cdot 10^{-5}$	3.07	0.15	14.28	2.09	0.09
$3.98 \cdot 10^{-5}$	3.04	0.11	18.86	2.40	0.06
$6.31 \cdot 10^{-5}$	2.93	0.05	38.43	2.49	0.04
$1.00 \cdot 10^{-4}$	2.91	0.04	49.74	2.54	0.03
$3.98 \cdot 10^{-4}$	2.91	0.03	56.30	2.61	0.03

A4.2 Simulations for variations of the metallicity

In Tables A4.3–A4.6, we summarize the results for the case of a constant fluctuation period while varying the metallicity.

Table A4.3: Results for the fluctuating mass accretion rate scenario described in Section (4.2.0.2). For these calculations, we assumed a initial accretion rate of $\dot{M}_0 = 10^{-6}$ $\mathrm{M}_\odot\,\mathrm{yr}^{-1}$ and a period of $50,000$ years, to observe the behavior when the metallicity is varied.

$Z = 0.001$					
Amplitude $[M_\odot\,\mathrm{yr}^{-1}]$	M_{ZAMS} $[M_\odot]$	t_{ZAMS} [Myr]	$\langle\dot{M}\rangle\cdot 10^{-6}$ $[M_\odot\,\mathrm{yr}^{-1}]$	M_{tr} $[M_\odot]$	t_{tr} [Myr]
$1.00\cdot 10^{-6}$	3.25	1.50	1.50	1.45	0.29
$1.58\cdot 10^{-6}$	3.40	1.34	1.79	1.49	0.26
$2.51\cdot 10^{-6}$	3.57	1.15	2.23	1.52	0.23
$3.98\cdot 10^{-6}$	3.81	0.94	3.00	1.52	0.19
$6.31\cdot 10^{-6}$	4.20	0.75	4.25	1.60	0.13
$1.00\cdot 10^{-5}$	4.64	0.59	6.20	1.70	0.10
$1.58\cdot 10^{-5}$	5.11	0.44	9.31	1.76	0.08
$2.51\cdot 10^{-5}$	5.29	0.33	12.90	1.80	0.07
$3.98\cdot 10^{-5}$	6.35	0.25	21.70	1.84	0.06
$6.31\cdot 10^{-5}$	6.18	0.18	29.50	1.87	0.05
$1.00\cdot 10^{-4}$	4.61	0.08	48.30	1.91	0.04
$1.00\cdot 10^{-3}$	4.20	0.03	108.00	2.01	0.02
$3.98\cdot 10^{-3}$	4.15	0.02	173.00	2.14	0.01

Table A4.4: Same as Table A4.3, but for metallicity $Z = 0.01$.

		$Z = 0.01$			
Amplitude $[M_\odot\,\mathrm{yr}^{-1}]$	M_{ZAMS} $[M_\odot]$	t_{ZAMS} [Myr]	$\langle \dot{M} \rangle \cdot 10^{-6}$ $[M_\odot\,\mathrm{yr}^{-1}]$	M_{tr} $[M_\odot]$	t_{tr} [Myr]
$1.00 \cdot 10^{-6}$	3.52	1.68	1.50	1.68	0.45
$1.58 \cdot 10^{-6}$	3.68	1.50	1.79	1.71	0.40
$2.51 \cdot 10^{-6}$	3.81	1.24	2.27	1.72	0.33
$3.98 \cdot 10^{-6}$	4.14	1.04	3.01	1.86	0.27
$6.31 \cdot 10^{-6}$	4.27	0.80	4.10	1.88	0.22
$1.00 \cdot 10^{-5}$	4.72	0.60	6.16	1.92	0.14
$1.58 \cdot 10^{-5}$	5.14	0.45	9.14	2.12	0.11
$2.51 \cdot 10^{-5}$	5.30	0.33	12.90	2.24	0.09
$3.98 \cdot 10^{-5}$	3.27	0.10	24.00	2.28	0.07
$6.31 \cdot 10^{-5}$	3.23	0.07	30.30	2.33	0.06
$1.00 \cdot 10^{-4}$	3.21	0.06	36.80	2.36	0.05
$1.00 \cdot 10^{-3}$	3.17	0.03	84.40	2.43	0.02
$3.98 \cdot 10^{-3}$	3.19	0.02	136.00	2.60	0.01

Table A4.5: Same as Table A4.3, but for metallicity $Z = 0.02$.

toprule		$Z = 0.02$			
Amplitude $[M_\odot\,\mathrm{yr}^{-1}]$	M_{ZAMS} $[M_\odot]$	t_{ZAMS} [Myr]	$\langle \dot{M} \rangle \cdot 10^{-6}$ $[M_\odot\,\mathrm{yr}^{-1}]$	M_{tr} $[M_\odot]$	t_{tr} [Myr]
$1.00 \cdot 10^{-6}$	3.31	1.54	1.51	1.77	0.52
$1.58 \cdot 10^{-6}$	3.86	1.61	1.77	1.83	0.46
$2.51 \cdot 10^{-6}$	3.45	1.08	2.27	1.84	0.38
$3.98 \cdot 10^{-6}$	3.78	0.92	3.02	1.94	0.31
$6.31 \cdot 10^{-6}$	4.81	0.90	4.22	2.07	0.25
$7.23 \cdot 10^{-6}$	3.87	0.61	4.68	2.07	0.23
$8.15 \cdot 10^{-6}$	4.12	0.60	5.21	2.01	0.21
$1.00 \cdot 10^{-5}$	5.18	0.70	5.94	1.98	0.18
$1.0725 \cdot 10^{-5}$	3.99	0.47	6.38	2.00	0.15
$1.145 \cdot 10^{-5}$	4.14	0.45	6.92	2.05	0.15
$1.29 \cdot 10^{-5}$	4.43	0.44	7.75	2.13	0.13
$1.58 \cdot 10^{-5}$	3.25	0.25	9.14	2.24	0.12
$2.51 \cdot 10^{-5}$	3.01	0.13	12.90	2.37	0.09
$3.98 \cdot 10^{-5}$	2.95	0.09	22.60	2.43	0.07
$6.31 \cdot 10^{-5}$	2.93	0.07	28.10	2.47	0.06
$1.00 \cdot 10^{-4}$	2.92	0.06	33.90	2.48	0.05
$1.00 \cdot 10^{-3}$	2.91	0.03	77.60	2.63	0.02
$3.98 \cdot 10^{-3}$	2.94	0.02	118.00	2.76	0.01

Table A4.6: Same as Table A4.3, but for metallicity $Z = 0.03$.

$Z = 0.03$					
Amplitude $[M_\odot\,\mathrm{yr}^{-1}]$	M_ZAMS $[M_\odot]$	t_ZAMS [Myr]	$\langle \dot{M} \rangle \cdot 10^{-6}$ $[M_\odot\,\mathrm{yr}^{-1}]$	M_tr $[M_\odot]$	t_tr [Myr]
$1.00 \cdot 10^{-6}$	3.13	1.42	1.50	1.80	0.54
$1.58 \cdot 10^{-6}$	3.23	1.25	1.79	1.85	0.47
$2.51 \cdot 10^{-6}$	3.43	1.07	2.28	1.93	0.41
$3.98 \cdot 10^{-6}$	3.74	0.91	3.03	1.94	0.32
$6.31 \cdot 10^{-6}$	3.62	0.64	4.10	2.12	0.26
$7.23 \cdot 10^{-6}$	3.85	0.60	4.73	2.12	0.24
$8.15 \cdot 10^{-6}$	4.09	0.59	5.22	2.10	0.23
$1.00 \cdot 10^{-5}$	3.82	0.47	5.99	1.99	0.18
$1.0725 \cdot 10^{-5}$	3.97	0.45	6.53	2.02	0.18
$1.145 \cdot 10^{-5}$	2.98	0.28	7.21	2.05	0.15
$1.29 \cdot 10^{-5}$	2.97	0.25	7.80	2.14	0.14
$1.58 \cdot 10^{-5}$	2.97	0.23	8.60	2.27	0.12
$2.51 \cdot 10^{-5}$	2.81	0.11	16.20	2.43	0.09
$3.98 \cdot 10^{-5}$	2.78	0.08	21.70	2.49	0.08
$6.31 \cdot 10^{-5}$	2.76	0.07	26.70	2.51	0.06
$1.00 \cdot 10^{-4}$	2.76	0.06	32.10	2.58	0.05
$1.00 \cdot 10^{-3}$	2.76	0.02	77.60	2.72	0.02
$3.98 \cdot 10^{-3}$	2.78	0.02	118.00	2.78	0.02

A5 Example of inlists and Fortran code

The following sections present the technical details of the models, outlining the setup and configuration adopted in this work.

A5.1 Inlist for MESA r23.05.1

This inlist was used to evolve a protostellar model up to the ZAMS assuming a constant accretion rate. The overall configuration remains essentially the same for the other accretion scenarios. The main differences arise from the additional physics included to model accretion variability, where fluctuations and an exponential decay of the accretion rate are implemented through the `run_star_extras` routines.

```
&star_job
    show_log_description_at_start   = .true.
```

```
    create_pre_main_sequence_model  = .true.

    save_model_when_terminate       = .true.
    save_model_filename             = 'start.mod'

    pgstar_flag                     = .true.
    pause_before_terminate          = .true.

    history_columns_file            = 'my_history_columns.list'
    profile_columns_file            = 'my_profile_columns.list'

    pre_ms_T_c                      = 1d5
/ ! end of star_job namelist

&kap
    Zbase                           = 0.02d0
    kap_file_prefix                 = 'gs98'
    use_Type2_opacities             = .true.
/ ! end of kap namelist

&controls
    stop_at_phase_ZAMS              = .true.
    max_model_number                = -1

    initial_mass                    = 1
    initial_z                       = 0.02d0

    photo_interval                  = 15
    profile_interval                = 15
    history_interval                = 15
    terminal_interval               = 10
    write_header_frequency          = 10

    log_directory                   = 'custom'
    max_num_profile_models          = 200
```

```
use_other_adjust_mdot          = .true.
accrete_same_as_surface        = .true.
x_ctrl(1)                      = 1d-6
! constant rate, see the subroutines in run_star_extras
! this has to be change in order to reproduce our results

varcontrol_target              = 1d-4
min_timestep_limit             = 1d-8

mixing_length_alpha            = 1.82
do_conv_premix                 = .true.
MLT_option                     = 'Henyey'

use_Ledoux_criterion           = .true.
alpha_semiconvection           = 1d-1
semiconvection_option          = 'Langer_85'

overshoot_scheme(:)            = 'step'
overshoot_zone_type(:)         = 'burn_H'
overshoot_zone_loc(:)          = 'core'
overshoot_bdy_loc(:)           = 'top'
overshoot_f(:)                 = 0.016
overshoot_f0(:)                = 0.004
```

A5.2 Code for `run_star_extras`

The following subroutine was implemented to include accretion in the stellar model, replacing the use of the standard `mass_change` control. This routine is added to the `run_star_extras` file, and the example shown below corresponds to the case of a constant accretion rate. The main advantage of this implementation is its flexibility, as it allows one to easily prescribe different accretion laws. In particular, this approach enables the inclusion of temporal fluctuations in the accretion rate as well as time-dependent decreasing accretion.

For this implementation to work, it is essential to assign the pointer `s%other_adjust_mdot => my_adjusted_mdot` inside the subroutine `extras_controls(id, ierr)`. During the relaxation phase, accretion is effectively suppressed in order to avoid numerical instabilities.

```fortran
subroutine my_adjusted_mdot(id, ierr)
    use star_def
    integer, intent(in)  :: id
    integer, intent(out) :: ierr
    type (star_info), pointer :: s
    real(dp) :: mdot0, t0, alpha, current_time, x_ctrl(1)
    ierr = 0
    call star_ptr(id, s, ierr)
    if (ierr /= 0) return
    ! Power-law accretion parameters
    mdot0 = s%x_ctrl(1) ! accretion rate [Msun/year]
    ! Current stellar age in years
    current_time = s%star_age
    ! Check whether the model is in the relaxation phase
    if (s%doing_relax) then
        s%mass_change = 1d-99   ! Very low accretion rate during relaxation
    else
        ! Apply the accretion prescription (constant in this case)
        s%mass_change = mdot0
    end if
end subroutine my_adjusted_mdot
```

For the case of a fluctuating accretion rate, we implemented a sinusoidal time-dependent prescription with period P and amplitude A.

```fortran
    A = s%x_ctrl(1)
    P = 50000 !years
    t = s%star_age
    mdot0 = 1d-6
     if (s%doing_relax) then
         s%mass_change = 1d-99
     else
         s%mass_change = mdot0 + A*sin(t/P)**2
     end if
```

For the case of a decreasing accretion rate, we implemented a time-dependent power-law prescription. The accretion rate decays as a function of stellar age according to an exponent α, with a characteristic normalization time t_0.

```fortran
mdot0 = s% x_ctrl(1)   !  accretion rate [Msun/year]
t0    = 0.3d6          ! Normalization time [years]
alpha = -1.d0          ! Decay exponent
t     = s% star_age    ! Current stellar age [years]

if (s% doing_relax) then
    s% mass_change = 1d-99
else
    s% mass_change = mdot0 * ((t + t0) / t0)**alpha
end if
```

A6 Kippenhahn diagrams for the constant accretion rate scenario

The following plots show all the Kippenhahn diagrams obtained for the constant accretion rate at each metallicity, allowing for a comparison of the internal structure of protostars with different metallicities at various accretion rates.

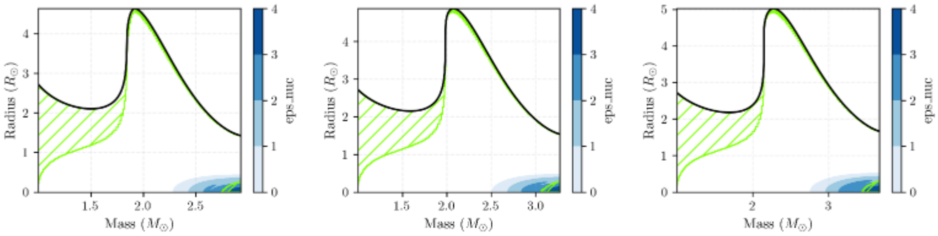

Z = 0.001

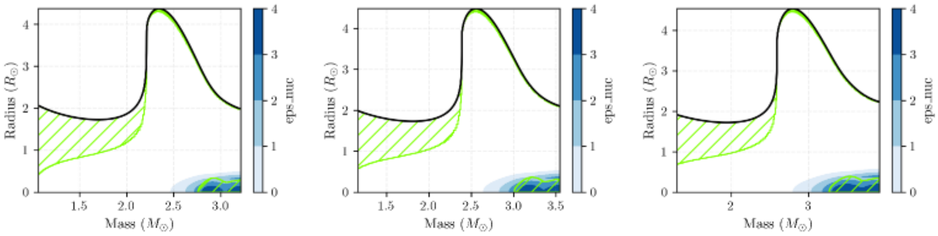

Z = 0.01

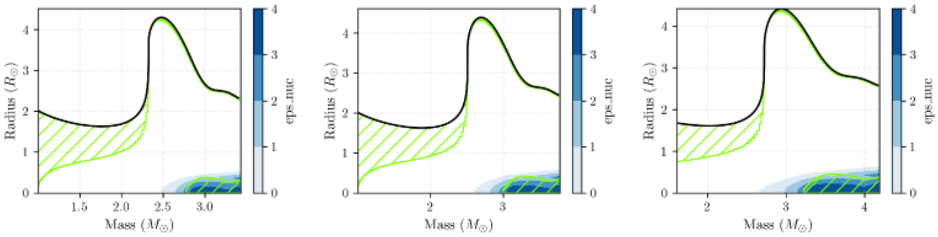

Z = 0.02

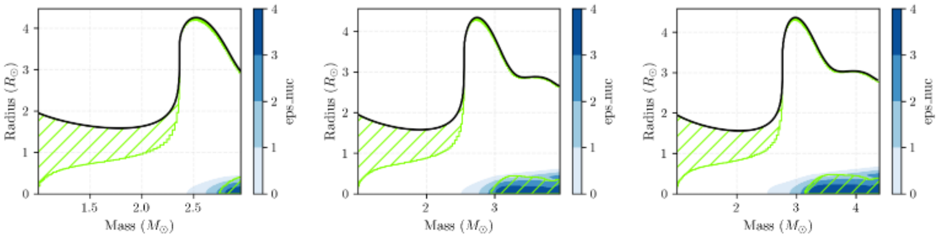

Z = 0.03

Figure A6.1: Kippenhahn diagrams. The first column corresponds to an accretion rate of $\dot{\mathrm{M}} = 1.00 \cdot 10^{-6} \mathrm{M}_\odot/\mathrm{yr}$, while the last column corresponds to $\dot{\mathrm{M}} = 2.51 \cdot 10^{-6} \mathrm{M}_\odot/\mathrm{yr}$.

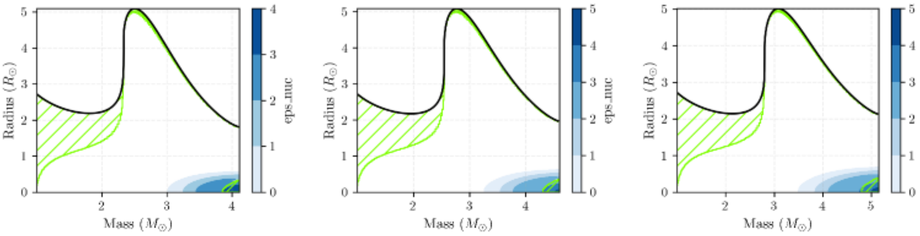

Z = 0.001

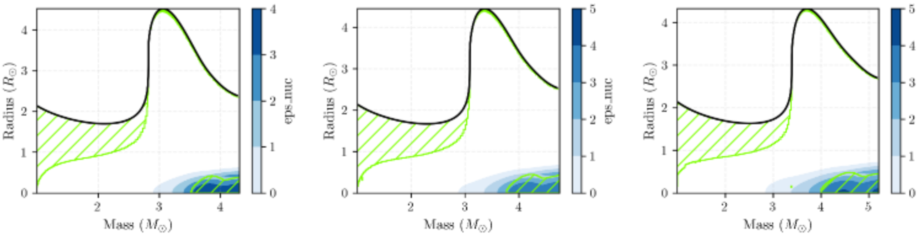

Z = 0.01

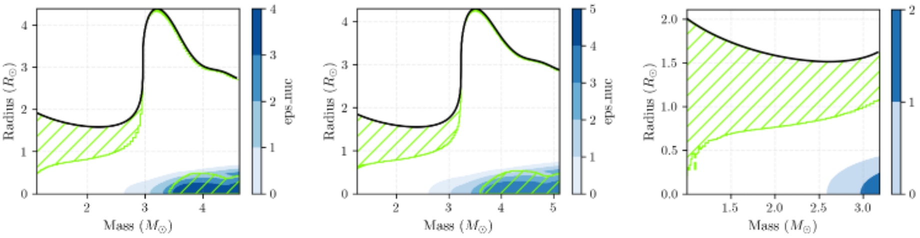

Z = 0.02

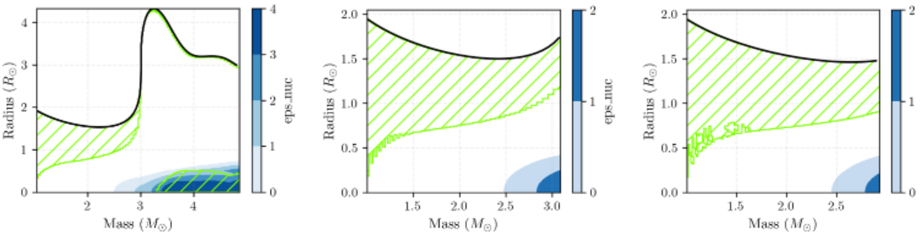

Z = 0.03

Figure A6.2: Kippenhahn diagrams. The first column corresponds to an accretion rate of $\dot{\mathrm{M}} = 3.98 \cdot 10^{-6}\mathrm{M}_\odot/\mathrm{yr}$, while the last column corresponds to $\dot{\mathrm{M}} = 1.00 \cdot 10^{-5}\mathrm{M}_\odot/\mathrm{yr}$.

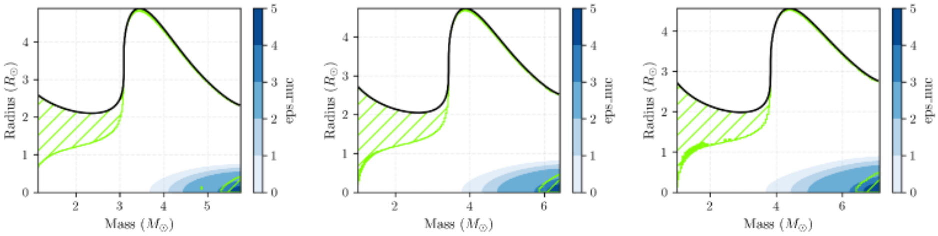

Z = 0.001

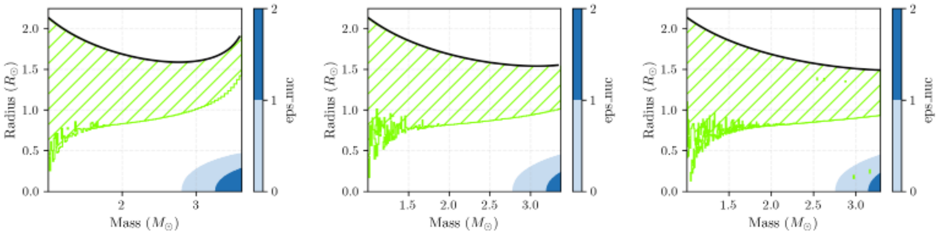

Z = 0.01

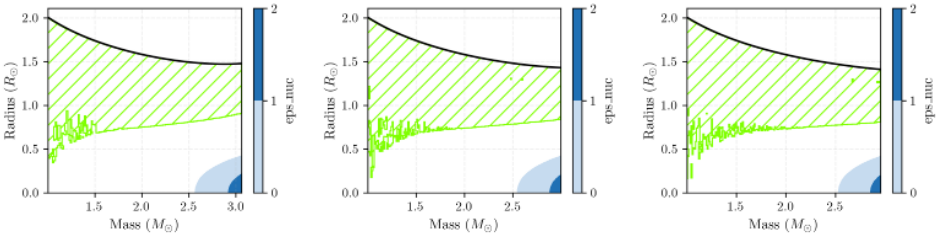

Z = 0.02

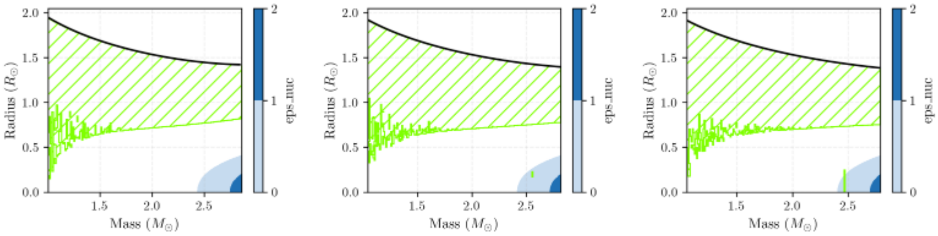

Z = 0.03

Figure A6.3: Kippenhahn diagrams. The first column corresponds to an accretion rate of $\dot{\mathrm{M}} = 1.58 \cdot 10^{-5}\mathrm{M}_\odot/\mathrm{yr}$, while the last column corresponds to $\dot{\mathrm{M}} = 3.98 \cdot 10^{-5}\mathrm{M}_\odot/\mathrm{yr}$.

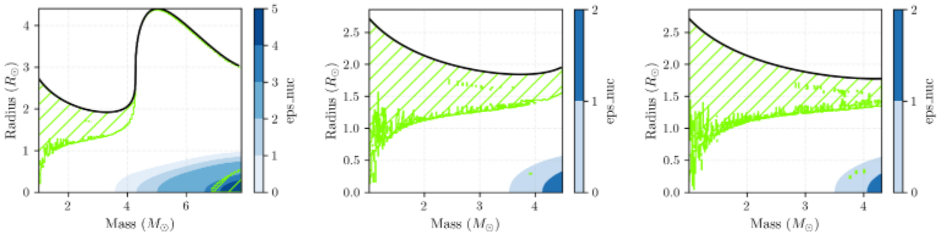

Z = 0.001

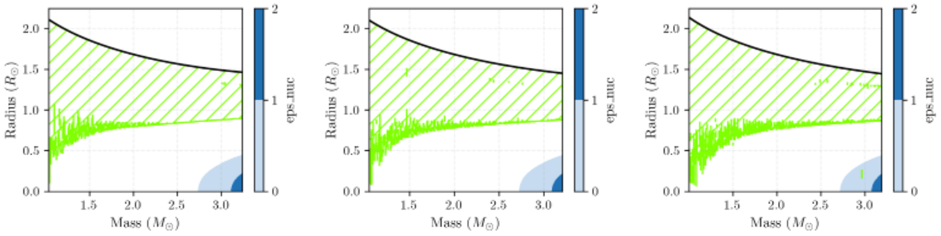

Z = 0.01

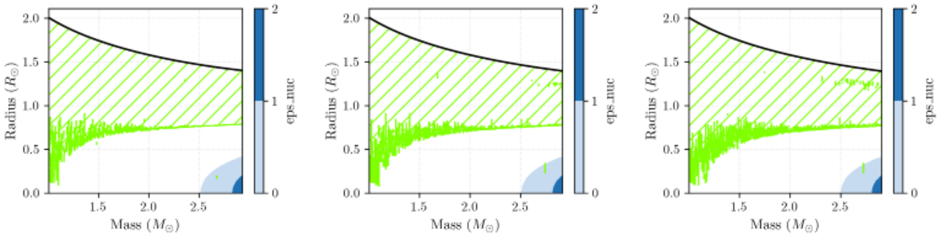

Z = 0.02

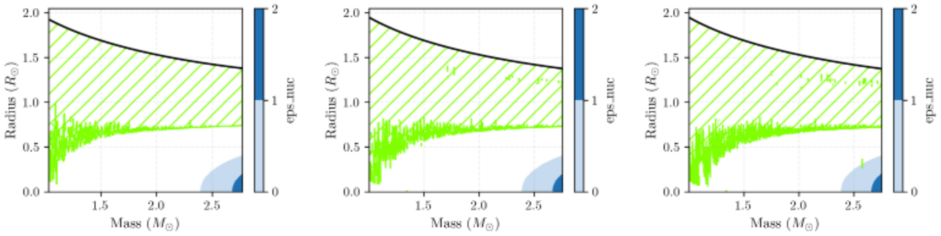

Z = 0.03

Figure A6.4: Kippenhahn diagrams. The first column corresponds to an accretion rate of $\dot{M} = 6.31 \cdot 10^{-5}\, M_\odot\,\mathrm{yr}^{-1}$, while the last column corresponds to $\dot{M} = 1.50 \cdot 10^{-4}\, M_\odot\,\mathrm{yr}^{-1}$.